Commun. Comput. Phys.
doi: 10.4208/cicp.OA-2025-0007

Vol. **39**, No. 1, pp. 78-118
January 2026

Vortex Spline Method for Two-Dimensional Rayleigh-Taylor Interfaces Between Inviscid and Perfect Dielectric Fluids with External Electric Fields

Wenxuan Guo[1] and Qiang Zhang[1,2,*]

[1] *Research Center for Mathematics, Beijing Normal University, Zhuhai 519087, P.R. China.*

[2] *Guangdong Provincial/Zhuhai Key Laboratory of IRADS, Beijing Normal-Hong Kong Baptist University, Zhuhai 519087, P.R. China.*

Received 8 January 2025; Accepted (in revised version) 30 March 2025

Abstract. Interfacial fluid instabilities are widespread in industrial applications. They often lead to mixing between different fluids and play an important role in industrial processes. How to control such interfacial instabilities between dielectric fluids by external electric fields have been actively explored. To understand the effects of external electric fields on the unstable interface and precisely control it, a numerical method capable of providing accurate results is indispensable and highly desired. In this paper, we present a numerical method for systems containing unstable material interfaces between incompressible, inviscid and perfect dielectric fluids in the presence of gravity and external electric fields in two dimensions. We extend the formulation of vortex sheets in the literature from hydrodynamics to electrohydrodynamics, and derive a numerical method in which the computation of both velocity and electric field is only conducted at the one-dimensional material interface. Non-uniform one-dimensional meshes are used to represent the interface shape, which captures the dominant features with fewer nodes. High-order regularization for the Birkhoff-Rott integral in the literature [1] is implemented to control the numerical instabilities. We implement a dynamic mesh adjustment algorithm to further improve the efficiency and robustness of numerical solutions. Validation studies on the convergence and accuracy are conducted.

AMS subject classifications: 65M38, 76B07, 76E25, 76M23

Key words: Vortex sheet, Rayleigh-Taylor instability, electrohydrodynamics, dielectric fluid, interfacial instability.

*Corresponding author. *Email addresses:* wenxuanguo@uic.edu.cn (W. Guo), mazq@uic.edu.cn (Q. Zhang)

1 Introduction

Interfacial flows between different fluids occur in a wide variety of natural phenomena and industrial applications. Under the effects of external forces, the material interface can become unstable and exhibit complicated dynamics. One of the classical examples is the instability that occurs when a light fluid supports a heavy fluid in a gravitational or acceleration field [2,3], namely the Rayleigh-Taylor instability (RTI). Small disturbances at an unstable Rayleigh-Taylor (RT) interface grow into large structures, and the fluids penetrate into each other. Since interfacial mixing in this process plays a key role in many engineering applications, it is essential to explore the approaches to controlling such an interface. One such approach is applying an external electric field to the interface between dielectric fluids [4–8]. To precisely control the evolution of the material interface, one needs to understand the dynamics of the material interface and investigate the various effects that the external electric field exerts on the interface. For this purpose, it is important and indispensable to conduct numerical simulations for this physical system. However, the unstable nature of the physical system leads to difficulties in the stability and accuracy of numerical methods. In this paper, we present a numerical method for studying the unstable material interface between incompressible, inviscid and perfect dielectric fluids in the presence of gravity and external electric fields in two dimensions. The presented method formulates both the velocity field and the electric displacement field in terms of "vortex sheets", which extends the vortex sheet methods from hydrodynamics in the absence of electric fields [9–15] to electrohydrodynamics which contains the interactions between gravity and electric fields.

Since the pioneering works of Rayleigh [2] and Taylor [16], the research on RTI has been active in the fields of theoretical, numerical, and experimental studies [11–13,17–38]. Following the exponential growth in the linear stage, nonlinear structures emerge at the material interface in the form of fingers. Accompanied by the nonlinear interactions and merging between adjacent fingers, the dynamics of the unstable interface eventually transitions into the turbulent stage. During this process, the evolution of the material interface, particularly the penetration between fluids that indicates the degree of interfacial mixing, is of great interest both to the researchers from the academic point of view and to the engineers aiming to control interfacial mixing in industrial applications. More details of the RTI and its applications can be found in the thorough and comprehensive reviews by Sharp [39] and Zhou [40,41].

Continuous mixing between fluids plays an important role in many industrial processes, e.g. the combustion between the fuel and the oxidizer. Therefore, precise control of unstable RT interfaces is highly desirable. For this reason, various methods for controlling the unstable material interface [42–44], including applying external electric fields to the interface between dielectric fluids, have been actively explored [3–8,45–48]. An experiment of continuum feedback control of a stable RT-type interface using electric fields was conducted by Melcher and Warren [4]. Numerical simulations on the RT-type interface in the presence of external electric fields were carried out by Cimpeanu et al. [47]

and by Yang et al. [48]. Cimpeanu *et al.* focused on the suppression effect on the finger growth from the horizontal electric field and presented a numerical experiment that used this effect to generate time-periodic interfacial oscillations [47]. Yang *et al.* additionally investigated RT unstable interfaces in a vertical electric field and numerically exhibited how electric fields changed the interfacial morphology [48].

In the absence of external electric fields, interfacial mixing between incompressible and inviscid fluids can be formulated in terms of vortex sheets. In this method, fluids are separated by a sharp and non-diffusive interface, across which the tangential velocity has a jump discontinuity due to the inviscid property of the fluids. Such a discontinuity in the fluid velocity is formulated as vorticities confined to the material interface. Conventionally, the numerical implementation of the vortex sheet formulation models the material interface by an array of point vortices along the interface and propagates these point vortices in a Lagrangian manner to determine the evolution of the entire system [9–15, 49, 50]. For studying interfacial mixing problems, the vortex sheet method has three distinct advantages over the usual Eulerian formulation. (1) It only needs to perform one-dimensional computation along the material interface, rather than two-dimensional computation solving the governing equations based on the Eulerian formulation. (2) In the vortex sheet method, its data structure directly represents the shape and location of the material interface, which is the most important information in interfacial mixing problems. Therefore, the method can accurately determine the shape and location of the interface. On the other hand, the numerical methods based on the Eulerian formulation usually need to construct or estimate these quantities from the two-dimensional grid-based data. Such constructions or estimations contain more numerical diffusion. (3) For systems with an unbound domain, which are common in theoretical considerations, no numerical boundaries are needed in the vortex sheet method, since the computation is solely and directly performed at the material interface and the far-field boundary conditions are fulfilled analytically. In contrast, since the numerical simulations in the Eulerian formulation can only be performed in a finite computational domain, one must introduce numerical boundaries for the finite computational domain and impose certain boundary conditions at these numerical boundaries. Numerical simulations for the classical RTI (i.e. without external electric fields) using vortex methods can be traced back to Baker *et al.* [10, 11] and Kerr [12], who respectively formulated the vortex sheet based on potential dipoles and local circulations. Tryggvason [20] developed a variation of this method based on the vortex-in-cell method [51] and applied it to simulations of the single-mode RT instability. This is later extended to simulations for bubble competition by Zufiria [23]. Rikanati *et al.* [14] used the vortex method for simulating the evolution of the multi-mode Richtmyer-Meshkov instability [52, 53], a related interfacial instability that is initiated by an impulsive force rather than gravitation, in the limit of two fluids of the same density. For systems with finite density ratios, Sohn conducted numerical experiments of Rayleigh-Taylor and Richtmyer-Meshkov instabilities and investigated the underlying dynamics for various density ratios [13]. In this paper, we consider a more complicated system in which the external electric field has an important impact on the dynamics of the unsta-

ble material interface. We extend the applicability of the vortex sheet formulation from classical hydrodynamics to electrohydrodynamics, and present a numerical method for electrohydrodynamics that inherits all the advantages from the classical vortex methods. One only needs to compute electrodynamics quantities on a one-dimensional "vortex sheet" that evolves with time. Therefore, the computation is very efficient. The presented numerical method also has the advantages in accurate determination of the interface shape and accurate evaluation of the electrical forces acting on the material interface. To the authors' knowledge, the numerical methods for electrohydrodynamics available in the literature are based on the Eulerian formulation. This is the first time that a numerical approach for electrohydrodynamics is established in the framework of vortex sheets.

In this paper, we consider a fluid system in the absence of viscosity and surface tension, a setting commonly investigated in theoretical studies. Although these approximations reduce the complexity of the system and make theoretical analysis tractable, the absence of these stabilizing mechanisms leads to difficulties in numerical simulations. The linear stability analysis shows that in such a system, the shorter the wavelength, the faster the finger grows. This property suggests that any small numerical errors introduced during the computation will be amplified into spurious fast-growing waves and can severely pollute the accuracy of the simulation, as demonstrated in [54–56]. To overcome this problem, Krasny regularized the point vortices as vortex "blobs", and showed that such regularization mitigates the instability of the vortex method [57]. Higher-order regularization methods for point vortices have been developed by Beale and Majda [58] and Bake and Beale [1]. By constructing proper regularization functions for the Birkhoff–Rott integral, they showed that the smoothing error caused by regularization is reduced to higher orders and accurate numerical solutions can be obtained. In this paper, we follow the regularization method presented in [1].

The remaining parts of this paper are structured as follows. In Section 2, we list the governing equations of RTI for incompressible, inviscid and perfect dielectric fluids in the presence of gravity and external electric fields. In Section 3, we formulate this problem in the framework of vortex sheets. Section 4 introduces the cubic spline representation for the material interface and provides the procedures for constructing the cubic spline. Section 5 displays the numerical implementation based on the vortex sheet formulation. Section 6 introduces a dynamic mesh adjustment to improve the efficiency of the numerical implementation. Section 7 is the validation studies. Section 8 presents numerical examples of an unstable RT interface controlled by various external electric fields. Section 9 is the conclusion.

2 Governing equations

We consider a material interface separating two immiscible and perfect dielectric fluids subject to gravity and external electric fields. Both fluids are inviscid, incompressible, and irrotational. Fluids 1 and 2 refer to the fluids below and above the material interface,

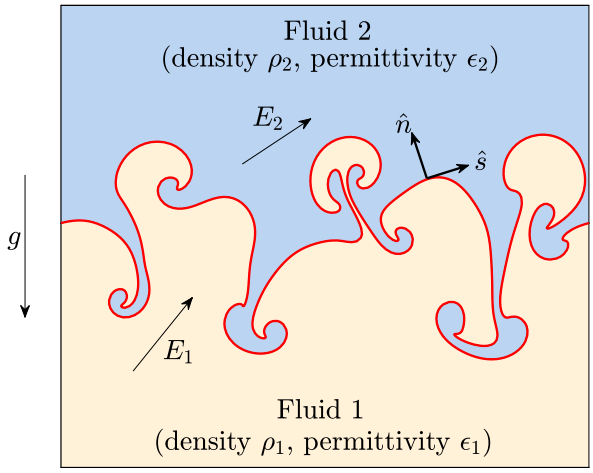

Figure 1: Schematic of the Rayleigh-Taylor instability problem in the presence of external electric fields. Two fluids of different densities and different electric permittivities are driven by both gravity and external electric fields.

respectively (see Fig. 1). For fluid i ($i=1,2$), the density and the electric permittivity are constant and denoted by ρ_i and ϵ_i, respectively. The vertical boundaries of the physical domain are infinite. This study focuses on systems with periodic boundaries in the horizontal direction, characterized by a width of 2π. Nevertheless, the proposed numerical method is also applicable to non-periodic systems. The fluids are considered static in the vertical far field. The surface tension is neglected. Driven by gravity and external electric fields, this system involves both hydrodynamics and electrodynamics. The hydrodynamics is governed by the Euler equations, and the electrodynamics is governed by Maxwell's equations. These two are coupled through the boundary conditions at the material interface between the fluids.

In each fluid phase i, the fluid motion is governed by the Euler equations, i.e.

$$\rho_i \boldsymbol{a_i} = -\nabla p_i - \rho_i g \hat{\boldsymbol{j}}, \quad i=1,2, \tag{2.1}$$

where $\boldsymbol{a_i}$ is the acceleration vector of fluid i, p_i is the pressure in fluid i, g is the magnitude of gravity, and $\hat{\boldsymbol{j}}$ is the vertical unit vector. We comment that the gravitational acceleration points downwards ($g>0$). In Eq. (2.1), the acceleration vector $\boldsymbol{a_i}$ is given by

$$\boldsymbol{a_i} \equiv \frac{\partial \boldsymbol{u_i}}{\partial t} + \boldsymbol{u_i} \cdot \nabla \boldsymbol{u_i}, \quad i=1,2, \tag{2.2}$$

where $\boldsymbol{u_i}$ is the velocity vector of fluid i. Due to the incompressible and irrotational

properties, the velocity vector $\boldsymbol{u_i}$ satisfies

$$\nabla\cdot\boldsymbol{u_i}=0,\quad i=1,2\qquad(\text{incompressible}),\tag{2.3a}$$

$$\nabla\times\boldsymbol{u_i}=0,\quad i=1,2\qquad(\text{irrotational}).\tag{2.3b}$$

The electric fields in the fluid bodies are determined by Maxwell's equations. Since the fluids are perfect dielectric, the electrical conductivity is zero and there are no free charges in the interior of the fluids. Then Gauss's law is written as

$$\nabla\cdot(\epsilon_i\boldsymbol{E_i})=0,\quad i=1,2,\tag{2.4}$$

where $\boldsymbol{E_i}$ is the electric vector of fluid i. Due to the absence of free charges, the dynamic currents and the induced magnetic fields are caused by polarization only. Therefore, the magnetic fields are negligible. Consequently, the Maxwell–Faraday equation reduces to

$$\nabla\times\boldsymbol{E_i}=0,\quad i=1,2.\tag{2.5}$$

To derive the governing equations in terms of vortex formulation in Section 3, we rewrite Eqs. (2.4) and (2.5) in terms of the electric displacement field $\boldsymbol{D_i}\equiv\epsilon_i\boldsymbol{E_i}$ as

$$\nabla\cdot\boldsymbol{D_i}=0\quad\text{and}\quad\nabla\times\boldsymbol{D_i}=0,\quad i=1,2.\tag{2.6}$$

At the material interface, we have the following boundary conditions. The fluid velocity is continuous in the normal direction, namely

$$(\boldsymbol{u_1}-\boldsymbol{u_2})\cdot\hat{\boldsymbol{n}}=0,\quad\text{at the interface},\tag{2.7}$$

where $\hat{\boldsymbol{n}}$ is the normal unit vector at the interface. We consider that no free surface charges exist at the material interface. Then the normal component of the electric displacement field and the tangent component of the electric field are continuous:

$$(\boldsymbol{D_1}-\boldsymbol{D_2})\cdot\hat{\boldsymbol{n}}=0,\quad\text{at the interface},\tag{2.8a}$$

$$(\boldsymbol{E_1}-\boldsymbol{E_2})\cdot\hat{\boldsymbol{s}}=\Big(\frac{\boldsymbol{D_1}}{\epsilon_1}-\frac{\boldsymbol{D_2}}{\epsilon_2}\Big)\cdot\hat{\boldsymbol{s}}=0,\quad\text{at the interface},\tag{2.8b}$$

where $\hat{\boldsymbol{s}}$ is the tangential unit vector. In the absence of surface tension, the normal stress is continuous:

$$\hat{\boldsymbol{n}}\cdot(\mathcal{T}_1-\mathcal{T}_2)\cdot\hat{\boldsymbol{n}}=0,\quad\text{at the interface},\tag{2.9}$$

where the stress tensor $\mathcal{T}_i$ of fluid i is defined by

$$\mathcal{T}_i=-p_iI+\epsilon_i\boldsymbol{E_i}\otimes\boldsymbol{E_i}-\frac{1}{2}\epsilon_i|\boldsymbol{E_i}|^2I+\frac{1}{2}|\boldsymbol{E_i}|^2\frac{\partial\epsilon_i}{\partial\rho_i}\rho_iI\tag{2.10}$$

$$=-p_iI+\frac{1}{\epsilon_i}\boldsymbol{D_i}\otimes\boldsymbol{D_i}-\frac{1}{2\epsilon_i}|\boldsymbol{D_i}|^2I\tag{2.11}$$

and I is the identity matrix. The last term on the right-hand side of Eq. (2.10) vanishes since ϵ_i is constant. After substituting Eq. (2.11) into Eq. (2.9), we obtain

$$p_1 - p_2 = \frac{1}{\epsilon_1}\left[(\boldsymbol{D_1}\cdot\hat{\boldsymbol{n}})^2 - \frac{1}{2}|\boldsymbol{D_1}|^2\right] - \frac{1}{\epsilon_2}\left[(\boldsymbol{D_2}\cdot\hat{\boldsymbol{n}})^2 - \frac{1}{2}|\boldsymbol{D_2}|^2\right]. \tag{2.12}$$

Eq. (2.12) shows that the difference in fluid pressure across the material interface is balanced by that in electrical force. Hence, the hydrodynamics and the electrodynamics in the system are coupled through Eq. (2.12) at the material interface.

At the vertical far fields, the velocities of the fluids are zero, i.e.

$$\boldsymbol{u_1}(y=-\infty) = \boldsymbol{u_2}(y=\infty) = 0, \tag{2.13}$$

and the electric displacement fields approach the external electric displacement, i.e.

$$\boldsymbol{D_1}(y=-\infty) = D_1^{ext}, \quad \boldsymbol{D_2}(y=\infty) = D_2^{ext}. \tag{2.14}$$

In summary, in terms of fluid velocity and electric displacement, the governing equations in the interior of the fluids are given by Eqs. (2.1)–(2.3) and (2.6), the boundary conditions at the material interface are given by Eqs. (2.7), (2.8), and (2.12), and the boundary conditions at the vertical far fields are given by Eqs. (2.13) and (2.14). In the next section, we will convert these governing equations and boundary conditions to the framework of the vortex sheet model. The resulting equations will be the foundation for the numerical scheme presented in Section 5.

3 Vortex sheet method for dielectric RTI problems

The vortex sheet method is one of the numerical methods designed to tackle unstable interfacial problems that involve multiple fluids [9,10,59]. In the absence of external electric fields, this method has been adopted for studying the RTI driven by gravity or acceleration, the Richtmyer-Meshkov instability driven by incident shocks, the Kelvin–Helmholtz instability caused by velocity difference between fluids, etc [11–13, 60]. To the authors' knowledge, the vortex sheet method has never been adopted for RT systems that involve electrohydrodynamics due to its complexity. In this section, we will extend the vortex sheet method from hydrodynamic systems to electrohydrodynamic systems. We will derive the governing equations based on the vortex formulation of the velocity field and the electric displacement field in an RT system between inviscid, incompressible and perfect dielectric fluids.

3.1 Vortex formulation for electrohydrodynamic systems

In the classical RTI problem, namely, when external electric fields are absent, the evolution of the material interface is driven by gravity only. For an RT system of inviscid and

incompressible fluids, Helmholtz's theorem holds and no vorticity exists in the interior of each fluid [61]. However, based on Bjerknes' generalization of Kelvin's circulation theorem [62], vorticity is generated when the density gradient and the pressure gradient are not aligned, which occurs at the material interface between fluids of different densities. Therefore, for RT systems, vorticity is continuously generated by gravity and is confined to the material interface. In the vortex formulation, it is the vorticity at the material interface that continuously drives the evolution of the entire system, and the strength and distribution of the vorticity determine the velocity fields of the fluids by the Birkhoff–Rott integral. Hence, the vorticity along the material interface forms a vortex sheet that determines the dynamics of the entire system [9,11–13].

In an RT system in two dimensions, the strength of the vortex sheet γ is defined by the jump in the tangential fluid velocity across the material interface [15,20], namely

$$\gamma \equiv (\boldsymbol{u_1}-\boldsymbol{u_2})\cdot\hat{\boldsymbol{s}}. \tag{3.1}$$

The motion of the vortex sheet follows the average velocity of the fluids on the two sides, i.e.

$$\bar{\boldsymbol{U}} \equiv \frac{1}{2}(\boldsymbol{u_1}+\boldsymbol{u_2}), \tag{3.2}$$

which is determined by the Birkhoff–Rott integral

$$\bar{U}_x - i\bar{U}_y = \fint_L K(s,s')\gamma' ds'. \tag{3.3}$$

Here the symbol $\fint$ denotes the Cauchy principal value of an integral, s denotes the arclength coordinate along the vortex sheet, and s' is the dummy variable in the integration. When the material interface is 2π-periodic in the horizontal direction, the integral in Eq. (3.3) is evaluated along one period of the vortex sheet L, and the kernel

$$K(s,s') = \frac{1}{4\pi i}\cot\left(\frac{z(s)-z(s')}{2}\right), \tag{3.4}$$

where $z = x+iy$ is the complex notation of the vortex sheet location. We comment that the evaluation of the average velocity, given by the line integral in Eq. (3.3), only requires quantities at the vortex sheet, i.e. the location z and the strength γ of the vortex sheet. As we will show later, this property allows us to reduce the numerical computation from the entire two-dimensional domain to the one-dimensional vortex sheet.

For an RT system that consists of inviscid, incompressible and perfect dielectric fluids with external electric fields, the velocity field can still be formulated by vortex sheets and determined by Eq. (3.3). This is because the external electric fields do not apply any body force in the interior of the fluids (see Eq. (2.1)) but exert a surface force only at the material interface (see Eq. (2.12)). Therefore, Helmholtz's theorem still holds in the interior regions and the vortex sheet formulation is applicable to the velocity field. However, this

system is more complicated than the one in the classical RTI problems, since it involves the electric displacement field and its interplay with the motion of the material interface. To evaluate the electrical force at the material interface given by Eq. (2.12), one needs to additionally compute the electric displacement field. If the electric displacement field could be formulated into "vortex sheets" similar to the velocity field, the computation of the electric displacement field would be only conducted along the one-dimensional vortex sheet as well. In that case, the dynamics of the entire system could again be formulated in terms of quantities at the one-dimensional "vortex sheets". We now show this indeed can be achieved.

The vortex sheet formulation is applicable to the velocity field because the velocity field has the following important properties. (1) It is divergence-free in the interior of the fluids (see Eq. (2.3a)). (2) It is rotation-free in the interior of the fluids (see Eq. (2.3b)). (3) The normal component is continuous across the material interface (see Eq. (2.7)). Note that the electric displacement field in our system also shares these three properties (see Eqs. (2.6) and (2.8a)). Such similarities suggest that the vortex formulation is also applicable to the electric displacement field in our system. Hence, we define the tangential difference in electric displacement across the material interface as the strength of the "vorticity" (i.e. the circulation) of electric displacement, namely

$$\beta \equiv (\boldsymbol{D_1} - \boldsymbol{D_2}) \cdot \hat{\boldsymbol{s}}. \tag{3.5}$$

Similar to the velocity field, the "vorticity" of the electric displacement field resides only at the material interface. Therefore, the "vorticity" of electric displacement can also be formulated in terms of a "vortex sheet" that coincides with the material interface, and β is the strength of the electric displacement "vortex sheet". We comment that the circulation of electric displacement only occurs when there is a dielectric jump across the interface, and the quantity β is the polarization charge induced by external electric fields due to this dielectric jump. The average electric displacement at the material interface is defined by

$$\bar{\boldsymbol{D}} \equiv \frac{1}{2}(\boldsymbol{D_1} + \boldsymbol{D_2}), \tag{3.6}$$

and can be determined from β by the Birkhoff–Rott integral. Under the periodic boundary conditions, the Birkhoff–Rott integral gives

$$\bar{D}_x - i\bar{D}_y = \fint_L K(s,s')\beta' ds' + D_x^{ext} - iD_y^{ext}, \tag{3.7}$$

where $K(s,s')$ is given by Eq. (3.4), and D_x^{ext} and D_y^{ext} are the horizontal and vertical components of the average electric displacement contributed by the external electric fields.

We would like to point out that there are two vortex sheets in the vortex formulation of our system, one for the velocity field whose strength is quantified by γ and the other for the electric displacement field whose strength is quantified by β. However, both vortex sheets are confined to the same material interface and therefore have the same location and the

same shape as the material interface. Based on this formulation, the governing equations can be expressed in terms of physical quantities at the material interface only, as we will show in the next subsection. Therefore, one only needs to evaluate and propagate these quantities at the one-dimensional interface instead of in the two-dimensional domain.

3.2 Governing equations of the dielectric RTI with external electric fields in the vortex formulation

We now rewrite the governing equations of the system in terms of physical quantities at the material interface based on the vortex formulation. Let α be the Lagrangian coordinate of the material interface. For the RT system governed by Eqs. (2.1)–(2.3), (2.6)–(2.8), and (2.12)–(2.14), at any given time t, the location $\boldsymbol{x}(s(\alpha,t),t)\equiv(x,y)$, the velocity $\bar{\boldsymbol{U}}(s(\alpha,t),t)\equiv(\bar{U}_x,\bar{U}_y)$, and the electric displacement $\bar{\boldsymbol{D}}(s(\alpha,t),t)\equiv(\bar{D}_x,\bar{D}_y)$ of/at the material interface are determined by the following set of equations:

$$\frac{\mathrm{d}\boldsymbol{x}}{\mathrm{d}t}=\bar{\boldsymbol{U}}, \tag{3.8a}$$

$$\frac{d\Gamma}{dt}=2A\int_{s(\alpha^-)}^{s(\alpha^+)}\frac{d\bar{\boldsymbol{U}}}{dt}\cdot\hat{\boldsymbol{s}}ds'+(2Agy-F_\gamma-F_e)\Big|_{\alpha^-}^{\alpha^+},\ \text{for any segment } (\alpha^-,\alpha^+), \tag{3.8b}$$

$$\beta+2A_\epsilon\bar{\boldsymbol{D}}\cdot\hat{\boldsymbol{s}}=0, \tag{3.8c}$$

$$\bar{U}_x=-\fint_L K_x\gamma' ds',\quad \bar{U}_y=\fint_L K_y\gamma' ds', \tag{3.8d}$$

$$\bar{D}_x=-\fint_L K_x\beta' ds'+D_x^{ext},\quad \bar{D}_y=\fint_L K_y\beta' ds'+D_y^{ext}. \tag{3.8e}$$

Here

$$\Gamma=\int_{s(\alpha^-)}^{s(\alpha^+)}\gamma(s',t)ds', \tag{3.9a}$$

$$K_x=\frac{1}{4\pi}\frac{\sinh(y-y')}{\cosh(y-y')-\cos(x-x')},\quad K_y=\frac{1}{4\pi}\frac{\sin(x-x')}{\cosh(y-y')-\cos(x-x')}, \tag{3.9b}$$

$$F_\gamma=-\frac{A}{4}\gamma^2,\quad F_e=\frac{\epsilon_2-\epsilon_1}{\epsilon_1\epsilon_2(\rho_1+\rho_2)}\left(\bar{D}_x^2+\bar{D}_y^2-\frac{\beta^2}{4}\right), \tag{3.9c}$$

$$A=(\rho_2-\rho_1)/(\rho_2+\rho_1),\quad A_\epsilon=(\epsilon_2-\epsilon_1)/(\epsilon_2+\epsilon_1). \tag{3.9d}$$

In Eqs. (3.8b) and (3.9a), α^- and α^+ are the Lagrangian coordinates of the starting and ending points of an arbitrary interface segment, and Γ is the vorticity resided in the segment. The definitions of γ and β are given by Eqs. (3.1) and (3.5), respectively.

Eq. (3.8a) is the propagation equation for the interface location. Eqs. (3.8d) and (3.8e) are directly from the Birkhoff–Rott integrals given by Eqs. (3.3) and (3.7). We comment that Eqs. (3.8a) and (3.8d) are identical to the governing equations in the classical RT system

and do not explicitly involve electrodynamics. However, the effects of electrodynamics enter the solutions of Eq. (3.8) via the distribution of polarization charge, which affects the vorticity along the interface. The former is determined by Eq. (3.8c) and the latter by Eq. (3.8b). Readers may refer to Appendix A for the derivation of Eqs. (3.8b) and (3.8c). Note that the average velocity $\bar{\boldsymbol{U}}$ and the average electric displacement $\bar{\boldsymbol{D}}$, expressed as integrals by Eqs. (3.8d) and (3.8e), also appear in the differential equations (Eqs. (3.8a) and (3.8b)). Hence, Eqs. (3.8a)–(3.8e) constitute a coupling integro-differential equation system.

3.3 Governing equations for non-periodic systems

In Sections 3.1 and 3.2, we presented the governing equations for RT systems with periodic horizontal boundaries. However, in some RTI problems, the horizontal boundaries are non-periodic and the motion of a closed material interface is of interest. To obtain the governing equations for such cases, one only need to replace the Biot-Savart kernel in the Birkhoff–Rott integrals of Eqs. (3.3) and (3.7) with

$$K(s,s')=\frac{1}{2\pi i}\frac{1}{z(s)-z(s')} \tag{3.10}$$

and evaluate the integrals along the entire interface. Consequently, the kernels K_x and K_y in Eq. (3.9b) are replaced by

$$K_x=\frac{1}{2\pi}\frac{y-y'}{(x-x')^2+(y-y')^2} \quad \text{and} \quad K_y=\frac{1}{2\pi}\frac{x-x'}{(x-x')^2+(y-y')^2}. \tag{3.11}$$

4 Discretization and cubic spline representation

To numerically solve Eq. (3.8), i.e. the governing equations for an RT system of perfect dielectric fluids in the presence of external electric fields in the framework of the vortex sheet, we divide one period of the material interface into N segments with $N+1$ points (see Fig. 2). For a point i ($0\le i\le N$) at the location $\boldsymbol{x}_i\equiv(x_i,y_i)$, $\bar{\boldsymbol{U}}_i$, $\bar{\boldsymbol{D}}_i$, and β_i are the quantities associated with that point. The periodic boundary conditions give $x_N=x_0+2\pi$, $y_N=y_0$, $\bar{\boldsymbol{U}}_N=\bar{\boldsymbol{U}}_0$, $\bar{\boldsymbol{D}}_N=\bar{\boldsymbol{D}}_0$, and $\beta_N=\beta_0$. For a segment i ($0\le i\le N-1$) with points i and $i+1$ being the endpoints, its arclength is denoted by Δs_i and the segment carries the local circulation of velocity Γ_i. These notations are illustrated in Fig. 2. We comment that, although the velocity field and the electric displacement field are both represented in the formulation of vortex sheets, the computed variables are chosen differently in our numerical scheme. For the electric displacement field, we compute at each point the polarization charge β, namely the "vortex strength" of electric displacement. This is because β occurs explicitly in Eqs. (3.8b) and (3.8c) (note that F_e in Eq. (3.8b) contains β). To solve these two equations, it is necessary to evaluate the value of β at each point. On the other hand, for the velocity field, we propagate the local circulation of velocity Γ in each segment by Eq. (3.8b), instead

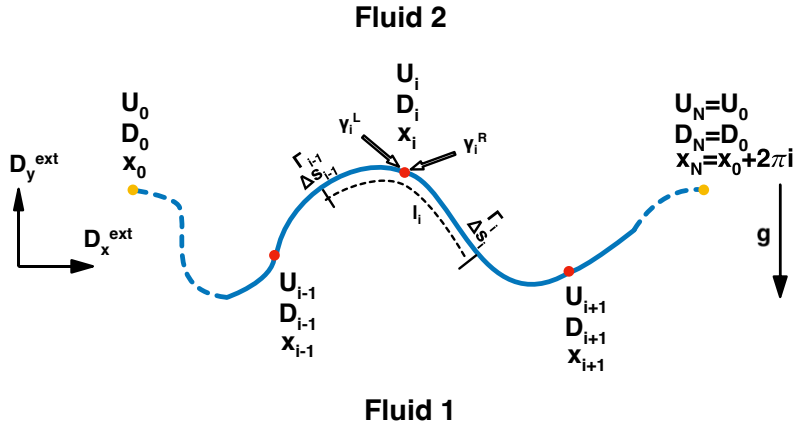

Figure 2: Discretized variables along the material interface. In particular, $\boldsymbol{x}_i$, $\bar{\boldsymbol{U}}_i$ and $\bar{\boldsymbol{D}}_i$ are variables for point i, and Δs_i and Γ_i are variables for segment i.

of the vortex strength γ at each point. The reasons are two-fold: (1) To propagate γ directly, one needs to evaluate the tangential derivatives in $\bar{\boldsymbol{U}}$, F_γ and F_e (see Eq. (A.11)). However, accurate numerical evaluation for such derivatives will be difficult for a material interface with a complicated shape that occurs commonly in RTI problems. On the other hand, to propagate Γ by Eq. (3.8b), one only needs to compute the difference of F_γ and that of F_e between the two endpoints of a segment, which are straightforward to calculate. (2) Eq. (3.8b) can be discretized into a conservative form for the vorticity Γ. Since the motion of the material interface is driven by Γ in the vortex formulation, the conservation of Γ is highly desired in the numerical computation.

Since the RT interface commonly evolves into a complicated shape at late times, it is crucial to establish a precise representation of the interface shape. This will lead to three improvements: (1) It can capture a material interface with a complicated shape better. (2) It gives a more accurate evaluation for Eqs. (3.8d) and (3.8e), since they are in the form of line integrals along the material interface. (3) It provides more accurate estimations for the arclength of segments and for the tangential direction at the material interface, which are essential in the computation of Eqs. (3.8b) and (3.8c). We will adopt the cubic spline method to achieve these purposes. In our vortex spline method, the shape of the material interface is represented by a cubic spline that is C^2-continuous along the material interface. This provides an accurate estimation of the tangential direction and a better representation of complicated interface shapes such as spiral roll-ups.

Let the interface have a set of points $\{(x_i,y_i)\}$ on a parametric curve $\boldsymbol{x}(s)=(x(s),y(s))$ in two dimensions, where s is the arclength coordinate along the material interface. Using s as the parameter, we construct a cubic spline for the curve (x,y). For each segment i, x, y and s must satisfy the relation $\Delta s_i = s(x_{i+1},y_{i+1}) - s(x_i,y_i) = \int_{s_i}^{s_{i+1}} \left[\left(\frac{\partial x}{\partial s}\right)^2 + \left(\frac{\partial y}{\partial s}\right)^2 \right]^{1/2} ds$, where $s_i \equiv s(x_i,y_i)$. Here $x(s)$ is the cubic spline function constructed for the x-coordinate,

i.e. a piecewise cubic polynomial in each subinterval $[s_i,s_{i+1}]$ that satisfies $x(s_i)=x_i$ and C^2-continuity at $s=s_i$. Similarly, $y(s)$ is the cubic spline function for the y-coordinate. Since the expressions of $x(s)$ and $y(s)$ depend on the values of $\{s(x_i,y_i)\}$, the above equation is a nonlinear equation for s. We solve this equation iteratively by applying $\Delta s_i^{(j+1)}=\int_{s_i^{(j)}}^{s_{i+1}^{(j)}}\left[\left(\frac{\partial x^{(j)}}{\partial s}\right)^2+\left(\frac{\partial y^{(j)}}{\partial s}\right)^2\right]^{\frac{1}{2}}ds$ until convergence, where j is the iteration index, the initial arclength of each segment is approximated by $\Delta s_i^{(0)}=\sqrt{(x_{i+1}-x_i)^2+(y_{i+1}-y_i)^2}$, and the arclength coordinate is updated by $s_i^{(j)}=\sum_{n=0}^{i-1}\Delta s_i^{(j)}$ in each iteration. We comment that $x^{(j)}(s)$ and $y^{(j)}(s)$ are the cubic spline functions constructed based on $\{s_i^{(j)}\}$. Therefore, the explicit expressions of $\frac{\partial x^{(j)}}{\partial s}$ and $\frac{\partial y^{(j)}}{\partial s}$ are available in the $(j+1)$th iteration. The following (Algorithm 1) is the pseudo-code of the interface shape construction in the vortex spline method:

Algorithm 1: Construction of a cubic spline for the interface shape

initial estimation for the arclength of each segment:
$\Delta s_i^{(0)}=\sqrt{(x_{i+1}-x_i)^2+(y_{i+1}-y_i)^2}$ for all i;
initial estimation for the arclength coordinate of each discrete point:
$s_i^{(0)}=\sum_{n=0}^{i-1}\Delta s_i^{(0)}$ for all i;
$j=0$;
repeat
  construct the cubic spline functions $x^{(j)}(s)$ and $y^{(j)}(s)$ based on the arclength $\{s_i^{(j)}\}$ such that $x^{(j)}(s_i^{(j)})=x_i$ and $y^{(j)}(s_i^{(j)})=y_i$ for all i;
  update the arclength of each segment:
  $\Delta s_i^{(j+1)}=\int_{s_i^{(j)}}^{s_{i+1}^{(j)}}\sqrt{(\frac{\partial x^{(j)}}{\partial s})^2+(\frac{\partial y^{(j)}}{\partial s})^2}ds$ for all i;
  update the arclength coordinate of each discrete point:
  $s_i^{(j+1)}=\sum_{n=1}^{i-1}\Delta s_i^{(j+1)}$ for all i;
  $j=j+1$;
until $\Delta s_i^{(j)}$ *is convergent*;

The procedure of cubic spline construction above determines the arclength coordinate s_i for each point (x_i,y_i), the arclength $\Delta s_i=s_{i+1}-s_i$ for each segment i, and the cubic spline functions $x(s)$ and $y(s)$ of the interface.

Fig. 3 demonstrates how a cubic spline can provide a more accurate representation for the complicated shape of a material interface. In Fig. 3a, the interface shape is represented by straight lines that connect adjacent points, while in Fig. 3b, the interface shape is represented by cubic spline segments. Both simulations are for the same system of $A=0.05$ and use 400 segments. Fig. 3 displays the portion of the material interface in the area $1\leq kx\leq 2$ and $-0.7\leq ky\leq 0.5$, which is near the center of a vortex structure. Fig. 3 clearly

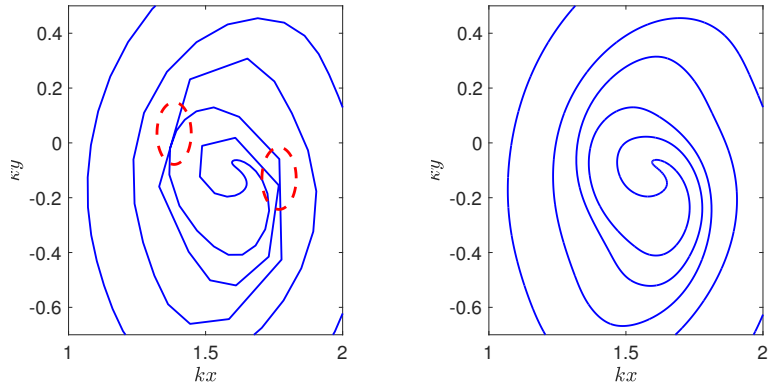

Figure 3: Comparison of a material interface represented by (a) straight-line segments and (b) cubic spline segments. The figures show that the cubic spline construction provides a more realistic representation for the shape of the material interface and avoids intersections at the interface, which occur in the straight-line representation (see the inside of the dashed red ellipses in figure (a)).

shows that the cubic spline representation provides a more realistic description of the interface shape than the straight-line segment representation for the same number of discrete points on the material interface. Furthermore, Fig. 3a shows that the material interface represented by straight-line segments intersects with itself near the center of the vortex structure (see the inside of the dashed red ellipses). Hence, the material interface represented by straight-line segments is no longer valid and the numerical simulation terminates shortly after. Fig. 3b shows no intersections at the material interface based on the cubic spline representation.

During the cubic spline construction, one needs to solve two tridiagonal matrices of size N-by-N to determine the coefficients of the cubic spline in each iteration. In practice, three iterations are usually sufficient for the cubic spline to converge. By using the Thomas algorithm, the complexity of solving these tridiagonal matrices is only $O(N)$. Since the evaluation of the Birkhoff–Rott integrals has a complexity of $O(N^2)$ and the cubic spline construction only has a lower complexity of $O(N)$, the portion of computational time spent on the latter does not play an important role in the efficiency of the numerical scheme.

Baker et al. [63] showed that singularity occurs at an RT interface in the vortex sheet formulation, namely the curvature can become infinite at one or more points along the interface at a critical time. To continue numerical simulations beyond the critical time, regularization of the Birkhoff–Rott integral has to be applied [1,57,58]. The application of regularization smooths the singularity of the material interface and gives an approximate solution for the interface motion beyond the critical time. As shown later in Section 5.2, we will implement such a regularization in our numerical method.

5 Numerical implementation

In this section, we describe the implementation of a numerical scheme for solving the governing equation (3.8) derived in Section 3 for the evolution of the material interface.

We decompose the external electric field into two: a horizontal electric field $\boldsymbol{E}_0 = E_0\hat{\boldsymbol{i}}$ and a vertical electric displacement field $\boldsymbol{D}_0 = D_0\hat{\boldsymbol{j}}$, where $\hat{\boldsymbol{i}}$ and $\hat{\boldsymbol{j}}$ are the horizontal and vertical unit vectors, respectively. The following (Algorithm 2) is the pseudo-code for solving an RTI problem from the initial time $t=0$ to the terminal time $t=T$ in the presence of external electric fields:

Algorithm 2: Steps for solving RTI with external electric fields

Initialization:
Step 1: initialize the external electric field by $D_x^{ext} = (\epsilon_1+\epsilon_2)E_0/2$ and $D_y^{ext} = D_0$;
Step 2: initialize the location $\boldsymbol{x}_i$, the velocity $\bar{\boldsymbol{U}}_i$ and the vorticity Γ_i of the interface;
Step 3: set time $t=0$;
Propagation (see Fig. 4 for details):
while $t<T$ **do**
  Step 4: determine the polarization charge β_i and the electric displacement $\bar{\boldsymbol{D}}_i$ at the interface;
  Step 5: solve $\boldsymbol{x}_i$, Γ_i and $\bar{\boldsymbol{U}}_i$ iteratively until convergence;
  Step 6: forward one time step by setting $t = t+\Delta t$;

In Steps 4 and 5 of Algorithm 2, we aim to solve a group of coupled nonlinear integro-differential equations, i.e. Eq. (3.8) for $\boldsymbol{x}$, Γ, $\bar{\boldsymbol{U}}$, β, and $\bar{\boldsymbol{D}}$. This approach involves the following *key procedures* (see Fig. 4):

P1: construct the shape of the material interface for evaluating the tangential unit vector $\hat{\boldsymbol{s}}$ in Eqs. (3.8b) and (3.8c) and the integrals in Eqs. (3.8d) and (3.8e);

P2: determine the average velocity $\bar{\boldsymbol{U}}$ and the average electric displacement $\bar{\boldsymbol{D}}$ at the material interface by evaluating Eqs. (3.8d) and (3.8e);

P3: determine the polarization charge β by solving Eq. (3.8c);

P4: propagate the location $\boldsymbol{x}$ of the material interface by Eq. (3.8a) and the vorticity Γ confined to the material interface by Eq. (3.8b).

In what follows, we provide the details of procedures P1–P4 in Sections 5.1–5.4, and then incorporate all these procedures into the numerical implementation in Section 5.5.

5.1 Construction of interface shape

This procedure is provided in Algorithm 1 already.

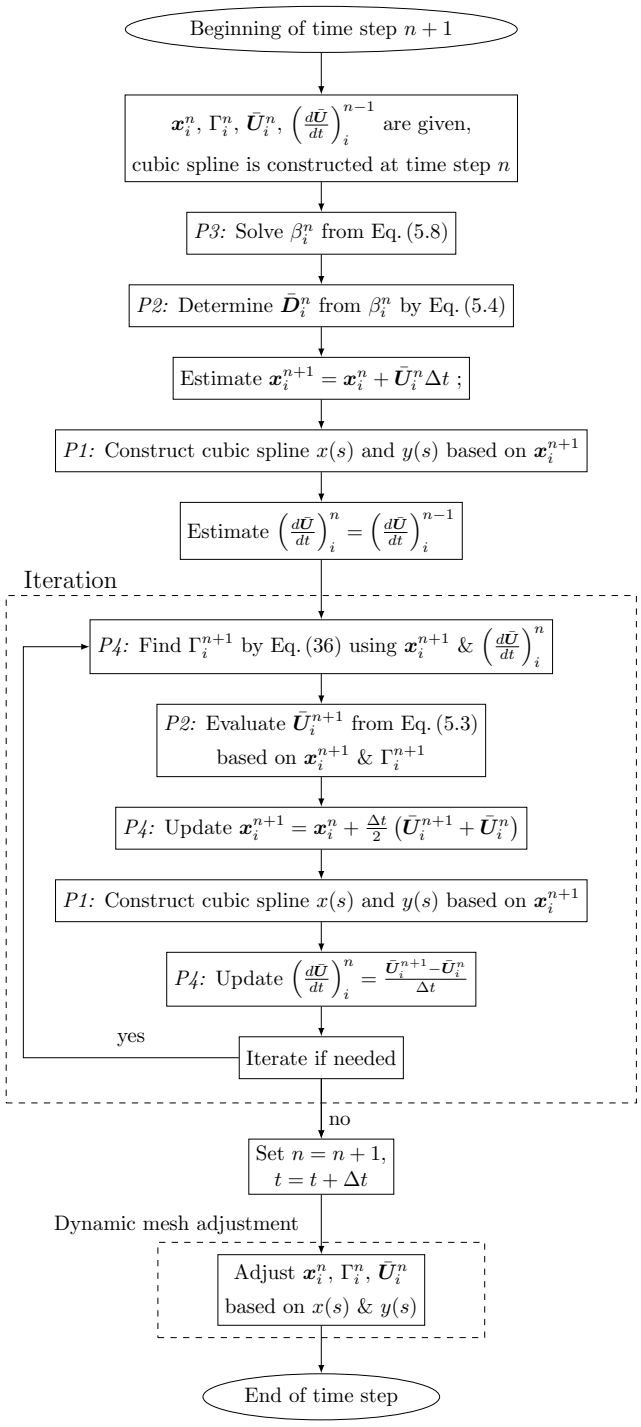

Figure 4: Flowchart for propagating the material interface by one time step Δt using the vortex spline method.

5.2 Numerical evaluations of the Birkhoff–Rott integrals

To solve the electrohydrodynamic system governed by Eq. (3.8), one needs to evaluate the average velocity $\bar{\boldsymbol{U}}$ by Eq. (3.8d) and the average electric displacement $\bar{\boldsymbol{D}}$ by Eq. (3.8e). However, computing Eqs. (3.8d) and (3.8e) directly is prone to failure in numerical simulations due to the following facts. Numerical analyses showed that short-wavelength instability of the vortex sheet led to difficulty in convergence [54,56]. Additionally, spurious short-wavelength modes caused by round-off errors in computers can drastically reduce the accuracy of computational results [56]. As aforementioned, singularity even occurs at the material interface in finite time [63]. To mitigate these problems, regularization methods for the Birkhoff–Rott integral are introduced [1,57,58]. The linear stability analysis showed that regularization diminished the short-wavelength instability and yielded numerically more tractable equations. Applying the regularization method in [1], we obtain the regularized version of Eqs. (3.8d) and (3.8e) by respectively replacing K_x and K_y with

$$K_{x,\delta}=K_x f\left(\frac{r}{\delta}\right) \quad \text{and} \quad K_{y,\delta}=K_y f\left(\frac{r}{\delta}\right). \tag{5.1}$$

Here δ is the regularization factor, $f=1+g_m$ and m denotes the order of the smoothing error caused by regularization. For systems with periodic horizontal boundaries, $r=\sqrt{2[\cosh(y-y')-\cos(x-x')]}$. For $m=1,3$, and 5, Baker and Beale [1] obtained

$$g_1(r)=-\exp\left(-r^2\right), \tag{5.2a}$$
$$g_3(r)=\left(-1+2r^2\right)\exp\left(-r^2\right), \tag{5.2b}$$
$$g_5(r)=\left(-1+4r^2-\frac{4}{3}r^4\right)\exp\left(-r^2\right). \tag{5.2c}$$

We approximate the regularized Eq. (3.8d) by the midpoint rule and have the sums:

$$\begin{aligned}(\bar{U}_x)_i&=-\sum_j (K_{x,\delta_v})_{i,j+\frac{1}{2}}\gamma_{j+\frac{1}{2}}\Delta s_j\\&=-\frac{1}{4\pi}\sum_j \frac{\sinh(y_i-y_{j+\frac{1}{2}})}{\cosh(y_i-y_{j+\frac{1}{2}})-\cos(x_i-x_{j+\frac{1}{2}})}f\left(\frac{r_{i,j+\frac{1}{2}}}{\delta_v}\right)\Gamma_j,\end{aligned} \tag{5.3a}$$
$$\begin{aligned}(\bar{U}_y)_i&=\sum_j (K_{y,\delta_v})_{i,j+\frac{1}{2}}\gamma_{j+\frac{1}{2}}\Delta s_j\\&=\frac{1}{4\pi}\sum_j \frac{\sin(x_i-x_{j+\frac{1}{2}})}{\cosh(y_i-y_{j+\frac{1}{2}})-\cos(x_i-x_{j+\frac{1}{2}})}f\left(\frac{r_{i,j+\frac{1}{2}}}{\delta_v}\right)\Gamma_j.\end{aligned} \tag{5.3b}$$

The location of the midpoint $(x_{j+\frac{1}{2}},y_{j+\frac{1}{2}})$ in the spline segment j is obtained from the cubic spline construction shown in Algorithm 1, $r^2_{i,j}=2[\cosh(y_i-y_j)-\cos(x_i-x_j)]$, and

$\gamma_{j+\frac{1}{2}}=\Gamma_j/\Delta s_j$. For Eq. (3.8e), we apply the trapezoidal rule and obtain

$$\begin{aligned}(\bar{D}_x)_i&=-\sum_j(K_{x,\delta_e})_{i,j}\beta_j\Delta l_j\\&=-\frac{1}{4\pi}\sum_j\frac{\sinh(y_i-y_j)}{\cosh(y_i-y_j)-\cos(x_i-x_j)}f\left(\frac{r_{i,j}}{\delta_e}\right)\beta_j\Delta l_j,\end{aligned}\tag{5.4a}$$

$$\begin{aligned}(\bar{D}_y)_i&=\sum_j(K_{y,\delta_e})_{i,j}\beta_j\Delta l_j\\&=\frac{1}{4\pi}\sum_j\frac{\sin(x_i-x_j)}{\cosh(y_i-y_j)-\cos(x_i-x_j)}f\left(\frac{r_{i,j}}{\delta_e}\right)\beta_j\Delta l_j,\end{aligned}\tag{5.4b}$$

where $\Delta l_j=\frac{1}{2}(\Delta s_{j-1}+\Delta s_j)$. A detailed and comprehensive study for the regularization and for the numerical quadrature of the Birkhoff–Rott integrals was conducted in [1].

Eqs. (5.3) and (5.4) are for systems with periodic horizontal boundaries. For non-periodic systems, the Biot-Savart kernels are given by Eq. (3.11) and regularized by Eq. (5.1) with $r=\sqrt{(x-x')^2+(y-y')^2}$ [1]. Then the velocity of the material interface is evaluated by

$$(\bar{U}_x)_i=-\frac{1}{2\pi}\sum_j\frac{y_i-y_{j+\frac{1}{2}}}{(y_i-y_{j+\frac{1}{2}})^2+(x_i-x_{j+\frac{1}{2}})^2}f\left(\frac{r_{i,j+\frac{1}{2}}}{\delta_v}\right)\Gamma_j,\tag{5.5a}$$

$$(\bar{U}_y)_i=\frac{1}{2\pi}\sum_j\frac{x_i-x_{j+\frac{1}{2}}}{(y_i-y_{j+\frac{1}{2}})^2+(x_i-x_{j+\frac{1}{2}})^2}f\left(\frac{r_{i,j+\frac{1}{2}}}{\delta_v}\right)\Gamma_j,\tag{5.5b}$$

and the average electric displacement at the material interface is evaluated by

$$(\bar{D}_x)_i=-\frac{1}{2\pi}\sum_j\frac{y_i-y_j}{(y_i-y_j)^2+(x_i-x_j)^2}f\left(\frac{r_{i,j}}{\delta_e}\right)\beta_j\Delta l_j,\tag{5.6a}$$

$$(\bar{D}_y)_i=\frac{1}{2\pi}\sum_j\frac{x_i-x_j}{(y_i-y_j)^2+(x_i-x_j)^2}f\left(\frac{r_{i,j}}{\delta_e}\right)\beta_j\Delta l_j,\tag{5.6b}$$

where $r_{i,j}^2=(x_i-x_j)^2+(y_i-y_j)^2$.

Using Eqs. (5.3)–(5.6), we can calculate the average velocity $\{\bar{\boldsymbol{U}}_i\}$ and the average electric displacement $\{\bar{\boldsymbol{D}}_i\}$ at the points $\{\boldsymbol{x}_i\}$ based on the cubic spline functions $x(s)$ and $y(s)$, the polarization charge $\{\beta_i\}$ and the local circulation of velocity $\{\Gamma_i\}$.

5.3 Determination of the electric displacement field

How the application of external electric fields affects the motion of the material interface is given by the term F_e in Eq. (3.8b). To evaluate this term, one needs to determine the polarization charge β from Eq. (3.8c). We discretize Eq. (3.8c) into

$$\beta_i+2A_e(\bar{D}_xs_x+\bar{D}_ys_y)_i=0,\quad\text{for } i=1,2,\cdots,N,\tag{5.7}$$

where the subscript $(\cdot)_i$ denotes that the quantities in the bracket are taken at point i, and $s_x \equiv \partial x/\partial s$ and $s_y \equiv \partial y/\partial s$ represent the horizontal and vertical components of the tangential unit vector $\hat{\boldsymbol{s}}$, respectively. By substituting Eq. (5.4) into Eq. (5.7), we obtain a set of linear equations for β_i, i.e.

$$\sum_{j=0}^{N-1} M_{ij}\beta_j = d_i, \quad \text{for } i=0,1,2,\cdots,N-1, \tag{5.8}$$

where

$$M_{ij} = \begin{cases} -\frac{A_\epsilon}{2\pi}\frac{\sinh\left(y_i-y_j\right)(s_x)_i-\sin\left(x_i-x_j\right)(s_y)_i}{\cosh\left(y_i-y_j\right)-\cos\left(x_i-x_j\right)} f\left(\frac{r_{i,j}}{\delta_e}\right)\Delta l_j, & i\neq j, \\ 1, & i=j, \end{cases} \tag{5.9a}$$

$$d_i = -2A_\epsilon\left[D_x^{ext}(s_x)_i + D_y^{ext}(s_y)_i\right]. \tag{5.9b}$$

Note that the coefficients of this linear system, namely $(s_x)_i$, $(s_y)_i$ and Δl_i, depend on the interface shape and are given by the cubic spline functions $x(s)$ and $y(s)$. By solving the system of linear equations given by Eq. (5.8), we obtain the values of $\{\beta_i\}$ and evaluate $\{(D_x)_i\}$ and $\{(D_y)_i\}$ from Eq. (5.4).

5.4 Propagation of the interface location and the velocity circulation

In the vortex spline method, we propagate the location $\boldsymbol{x}$ of the material interface by Eq. (3.8a) and the vorticity Γ at the material interface by Eq. (3.8b). Given the location $\{\boldsymbol{x}_i^n\}$ and the vorticity $\{\Gamma_i^n\}$ at the current time step n, these two quantities are propagated to the next time step $n+1$ by the discretized form of Eqs. (3.8a) and (3.8b):

$$\boldsymbol{x}_i^{n+1} = \boldsymbol{x}_i^n + \frac{\Delta t}{2}\left(\bar{\boldsymbol{U}}_i^{n+1} + \bar{\boldsymbol{U}}_i^n\right), \tag{5.10}$$

$$\begin{aligned}\Gamma_i^{n+1} = \Gamma_i^n + \Delta t\Bigg(&A\left[\left(\frac{d\bar{\boldsymbol{U}}}{dt}\right)_i^n\cdot\hat{\boldsymbol{s}}_i^n + \left(\frac{d\bar{\boldsymbol{U}}}{dt}\right)_{i+1}^n\cdot\hat{\boldsymbol{s}}_{i+1}^n\right]\Delta s_i^n + 2Ag\left(y_{i+1}^n - y_i^n\right) \\ &-\left[(F_\gamma)_{i+1}^n - (F_\gamma)_i^n\right] - \left[(F_e)_{i+1}^n - (F_e)_i^n\right]\Bigg).\end{aligned} \tag{5.11}$$

Here Δt is the size of the time step, and the superscript $(\cdot)^n$ denotes the value of a quantity at the time step n. In Eq. (5.11),

$$\left(\frac{d\bar{\boldsymbol{U}}}{dt}\right)_i^n = \frac{\bar{\boldsymbol{U}}_i^{n+1} - \bar{\boldsymbol{U}}_i^n}{\Delta t}, \tag{5.12}$$

$$(F_e)_i^n = \frac{\epsilon_2-\epsilon_1}{\epsilon_1\epsilon_2(\rho_1+\rho_2)}\left(\left[(\bar{D}_x)_i^n\right]^2 + \left[(\bar{D}_y)_i^n\right]^2 - \frac{\left(\beta_i^n\right)^2}{4}\right), \tag{5.13}$$

and $(F_\gamma)_i^n$ is evaluated as follows. Since vorticity can concentrate in certain regions of the RT interface, a steep slope of the vortex strength γ occurs [13]. To preserve numerical stability, we use the Godunov solver to compute the flux $(F_\gamma)_i^n$, namely,

$$(F_\gamma)_i^n = -\frac{A}{4}\max\left[(\gamma_{i-}^n)^2,(\gamma_{i+}^n)^2\right], \tag{5.14}$$

where

$$\gamma_{i-}^n = \min\left[\left(\gamma^{\mathrm{L}}\right)_i^n,0\right], \quad \gamma_{i+}^n = \max\left[\left(\gamma^{\mathrm{R}}\right)_i^n,0\right]. \tag{5.15}$$

Here $\left(\gamma^{\mathrm{L}}\right)_i^n \equiv \gamma(t=t^n,s=s_i^-)$ is the left state of γ at point i at the time step n, and $\left(\gamma^{\mathrm{R}}\right)_i^n \equiv \gamma(t=t^n,s=s_i^+)$ is the right state of γ at point i at the time step n (see Fig. 2). The states $\left(\gamma^{\mathrm{L}}\right)_i^n$ and $\left(\gamma^{\mathrm{R}}\right)_i^n$ are reconstructed from $\{\Gamma_i^n\}$ by the same approach as in the finite volume methods. For example, using the Godunov scheme [64] to reconstruct the left and right states of γ at point i gives

$$\left(\gamma^{\mathrm{L}}\right)_i^n = \Gamma_{i-1}^n/\Delta s_{i-1}^n \quad \text{and} \quad \left(\gamma^{\mathrm{R}}\right)_i^n = \Gamma_i^n/\Delta s_i^n, \tag{5.16}$$

which are estimated by the average vortex strengths in the left and right spline segments, respectively. For reconstruction with higher accuracy, one can refer to the MUSCL scheme [65] and the WENO scheme [66, 67].

We comment that Eqs. (5.3), (5.10), and (5.11) are strongly coupled because $\boldsymbol{x}_i^{n+1}$, Γ_i^{n+1}, and $\bar{\boldsymbol{U}}_i^{n+1}$ depend on each other: $\boldsymbol{x}_i^{n+1}$ is propagated by $\bar{\boldsymbol{U}}_i^{n+1}$ in Eq. (5.10); Γ_i^{n+1} depends on $\bar{\boldsymbol{U}}_i^{n+1}$ since $\left(\frac{d\bar{\boldsymbol{U}}}{dt}\right)_i^n$ in Eq. (5.11) has dependency on $\bar{\boldsymbol{U}}_i^{n+1}$ (see Eq. (5.12)); $\bar{\boldsymbol{U}}_i^{n+1}$ depends on $\boldsymbol{x}_i^{n+1}$ and Γ_i^{n+1} in the form of line integrals given by Eq. (5.3). We will apply an iterative method to solve this coupling system, which is discussed in the next subsection.

5.5 Procedures for propagating the system by one time step

At the beginning of the time step $n+1$, the quantities $\{\boldsymbol{x}_i^n\}$, $\{\Gamma_i^n\}$, $\{\bar{\boldsymbol{U}}_i^n\}$, and $\left\{\left(\frac{d\bar{\boldsymbol{U}}}{dt}\right)_i^{n-1}\right\}$ are known. We apply an iterative approach to propagate these quantities by one time step Δt. This is given by the following pseudo-code (Algorithm 3):

Algorithm 3: Procedures for propagating the system by Δt

Known: $\boldsymbol{x}_i^n$, Γ_i^n, $\bar{\boldsymbol{U}}_i^n$, and $\left(\frac{d\bar{\boldsymbol{U}}}{dt}\right)_i^{n-1}$

Initialization of iteration:

determine β_i^n from Eq. (5.8), and evaluate $\bar{\boldsymbol{D}}_i^n$ by Eq. (5.4);

estimate $\boldsymbol{x}_i^{n+1} = \boldsymbol{x}_i^n + \bar{\boldsymbol{U}}_i^n \Delta t$, construct $x(s)$ and $y(s)$ based on $\boldsymbol{x}_i^{n+1}$;

estimate $\left(\frac{d\bar{\boldsymbol{U}}}{dt}\right)_i^n = \left(\frac{d\bar{\boldsymbol{U}}}{dt}\right)_i^{n-1}$;

Iteration:

repeat

  determine Γ_i^{n+1} from Eq. (5.11) using $\boldsymbol{x}_i^{n+1}$ and $\left(\frac{d\bar{\boldsymbol{U}}}{dt}\right)_i^n$;

  evaluate $\bar{\boldsymbol{U}}_i^{n+1}$ by Eq. (5.3) based on $\boldsymbol{x}_i^{n+1}$ and Γ_i^{n+1};

  $\boldsymbol{x}_i^{n+1} = \boldsymbol{x}_i^n + \frac{\Delta t}{2}\left(\bar{\boldsymbol{U}}_i^{n+1} + \bar{\boldsymbol{U}}_i^n\right)$, construct $x(s)$ and $y(s)$ based on $\boldsymbol{x}_i^{n+1}$;

  $\left(\frac{d\bar{\boldsymbol{U}}}{dt}\right)_i^n = \frac{\bar{\boldsymbol{U}}_i^{n+1} - \bar{\boldsymbol{U}}_i^n}{\Delta t}$;

until *convergence*;

A flowchart for these procedures is shown in Fig. 4. This concludes the implementation of the vortex spline method.

6 Dynamic mesh for the material interface

The implementation shown in Section 5 uses a fixed number of cubic spline segments to represent the shape of the material interface. This is usually sufficient for numerical simulations of an unstable interface at early times. However, as time progresses, complicated structures appear at the unstable material interface. The material interface is stretched out to a much larger extent than the initial state, and the interface shape becomes much more complicated. Therefore, using a fixed number N of cubic spline segments to represent the shape of an unstable material interface eventually leads to a lack of resolution at late times. Even though one could discretize the initial material interface with a finer mesh (namely using a larger value of N) to delay the occurrence of under-resolution, this approach is inefficient for two reasons. (1) A finer mesh causes longer computation time and requires more computational efforts. Such additional costs are unnecessary since at early times the material interface is not stretched significantly. (2) The stretching at the material interface is nonuniform. The resolution in the vicinity of the stretched region still rapidly becomes insufficient even with a finer mesh, and it is impossible to determine the stretched region a priori for general cases. To resolve this issue, we introduce a procedure of dynamic mesh adjustment that efficiently refines the mesh in the vortex spline method during the numerical computation.

Given a material interface represented by a sequence of cubic spline segments, at the

end of each time step, we perform three procedures for each segment i:

Procedure 1: Examine whether the spline segment is too stretched or too curvy. The former is determined by whether the arclength Δs_i exceeds a threshold value Δs_c, and the latter is determined by whether $\cos^{-1}(\hat{\boldsymbol{s}}_i \cdot \hat{\boldsymbol{s}}_{i+1})$ exceeds a threshold value θ_c.

Procedure 2: If either criterion in Procedure 1 is met, split the spline segment into two by its midpoint. Note that the midpoint of every spline segment is already available when evaluating Eq. (5.3).

Procedure 3: Allocate the vorticity Γ_i in the pre-split spline segment to the two post-split segments. We comment that a straightforward interpolation may yield oscillations of the vortex strength γ and lead to numerical instability in the subsequent computation. To retain the monotonicity of γ between neighboring segments and avoid spurious oscillations during the allocation of Γ, we adopt the same idea of the MUSCL scheme [65]. Namely, γ in the pre-split segment is approximated by a linear function, and the derivative of γ is limited by a slope limiter. Consider a pre-split segment i which has the arclength Δs_i and holds the vorticity Γ_i. We first calculate the average vortex strength in segment j ($j=i-1,i,i+1$) by $\bar{\gamma}_j=\Gamma_j/\Delta s_j$. The left and right slopes of γ in segment i are estimated by

$$d_l=2\frac{\bar{\gamma}_i-\bar{\gamma}_{i-1}}{\Delta s_i+\Delta s_{i-1}} \quad \text{and} \quad d_r=2\frac{\bar{\gamma}_{i+1}-\bar{\gamma}_i}{\Delta s_{i+1}+\Delta s_i}. \tag{6.1}$$

The limited slope of γ in segment i is then given by

$$d=\text{minmod}(d_l,d_r), \tag{6.2}$$

where $\text{minmod}(\cdot)$ is the minmod slope limiter defined by

$$\text{minmod}(a,b)=\begin{cases}\min(a,b), & \text{if } a\geq 0,b\geq 0,\\ 0, & \text{if } ab<0,\\ \max(a,b), & \text{if } a\leq 0,b\leq 0.\end{cases} \tag{6.3}$$

Finally, the segment i is divided into two segments of equal arclength $\Delta s_i/2$ with the left (right) segment containing the vorticity Γ_i^L (Γ_i^R), where

$$\Gamma_i^L=\int_{-\frac{\Delta s_i}{2}}^{0}(\bar{\gamma}_i+ds)\,ds=\frac{1}{2}\Gamma_i-\frac{1}{8}d\Delta s_i,\ \Gamma_i^R=\Gamma_i-\Gamma_i^L=\frac{1}{2}\Gamma_i+\frac{1}{8}d\Delta s_i. \tag{6.4}$$

Once the local refinement of all spline segments is finished, we reevaluate all physical quantities based on the post-split segments. The pseudo-code of the dynamic mesh adjustment is as follows (Algorithm 4):

Algorithm 4: How to dynamically adjust the mesh

At the end of each time step n:

foreach *cubic spline segment* $(x(s),y(s))$ *where* $s\in[s_i^n,s_{i+1}^n]$ **do**
  if $\Delta s_i^n>\Delta s_c$ *or* $\cos^{-1}(\hat{\boldsymbol{s}}_i^n\cdot\hat{\boldsymbol{s}}_{i+1}^n)>\theta_c$ **then**
    $s_{i+\frac{1}{2}}^n=\frac{1}{2}(s_i^n+s_{i+1}^n)$;
    split the spline segment by its midpoint: $\boldsymbol{x}_p^n=\left(x(s_{i+\frac{1}{2}}^n),y(s_{i+\frac{1}{2}}^n)\right)$;
    interpolate the acceleration: $\left(\frac{d\bar{\boldsymbol{U}}}{dt}\right)_p^{n-1}=\frac{1}{2}\left[\left(\frac{d\bar{\boldsymbol{U}}}{dt}\right)_i^{n-1}+\left(\frac{d\bar{\boldsymbol{U}}}{dt}\right)_{i+1}^{n-1}\right]$;
    allocate the vorticity in the post-split segments $[s_i^n,s_{i+\frac{1}{2}}^n]$ and $[s_{i+\frac{1}{2}}^n,s_{i+1}^n]$ with Γ_i^L and Γ_i^R given by Eq. (6.4);
reconstruct the cubic spline $(x(s),y(s))$ based on the post-split mesh;
evaluate the average velocity $\{\bar{\boldsymbol{U}}_i^n\}$ at all points of the post-split mesh, based on the updated cubic spline $(x(s),y(s))$ and vorticity $\{\Gamma_i^n\}$;
proceed to the next time step.

The implementation of dynamic mesh adjustment in the vortex spline method is shown as the lower dashed box in Fig. 4. We comment that Krasny [68] developed a point insertion technique, in which the coordinates of the newly inserted point are determined by cubic polynomial interpolation based on the coordinates of four neighboring points. In our approach, the coordinates of the inserted point are determined from our basic construction of a cubic spline based on all points at the interface.

The arclength of the cubic spline segments gradually decreases as the refinement of the mesh continues. Therefore, the size of the time step Δt needs to be adjusted adaptively to avoid violating the Courant–Friedrichs–Lewy (CFL) condition. Eq. (3.8b) indicates that one needs to solve a local Riemann problem of γ at each point $\boldsymbol{x}_i$, and the CFL condition requires

$$\Delta t^n\cdot\max\left[-\frac{A}{2}\left(\gamma^{\mathrm{R}}\right)_i^n,-\frac{A}{4}\left(\left(\gamma^{\mathrm{L}}\right)_i^n+\left(\gamma^{\mathrm{R}}\right)_i^n\right)\right]<\Delta s_i^n, \tag{6.5a}$$

$$\Delta t^n\cdot\max\left[\frac{A}{2}\left(\gamma^{\mathrm{L}}\right)_{i+1}^n,\frac{A}{4}\left(\left(\gamma^{\mathrm{L}}\right)_{i+1}^n+\left(\gamma^{\mathrm{R}}\right)_{i+1}^n\right)\right]<\Delta s_i^n \tag{6.5b}$$

for all i. Here $\left(\gamma^{\mathrm{L}}\right)_i^n$ and $\left(\gamma^{\mathrm{R}}\right)_i^n$ are the values of γ at $s=s_i^-$ and $s=s_i^+$ at the time step n, respectively (see Eq. (5.16) for the example of the Godunov scheme). At the beginning of each simulation, an initial time step Δt^0 is assigned. Then we check whether the CFL condition is satisfied at the beginning of each time step. If the CFL condition is violated, we reduce Δt by half repeatedly until the CFL condition is satisfied, and then use Algorithm 3 to propagate the interface.

7 Validation studies

In this section, we will conduct validation studies of the vortex spline method. There are two key numerical parameters in the vortex spline method, namely the number of spline segments N used to represent the shape of the material interface and the magnitudes of the regularization factors (δ_v and δ_e). We will show that the vortex spline method gives convergent numerical solutions under these two numerical parameters. Since analytical solutions in the literature are valid only up to the weakly nonlinear regime [6,69], we conduct our validation studies in two stages. First, we validate the convergence of the vortex spline method up to the weakly nonlinear regime by comparing the obtained numerical results with the theoretical predictions. Second, we carry out convergence studies in the fully nonlinear regime. The velocity of the finger tip at the RT interface indicates how the fluids in the system penetrate into each other, which is the most important physical quantity people are interested in. Therefore, we will validate this quantity obtained from the numerical simulations.

For the convenience of analyzing and presenting the numerical results, we introduce the dimensionless length scales $\tilde{x}=kx$ and $\tilde{y}=ky$ and the dimensionless time scale $\tilde{t}=t\sqrt{kg}$. The densities and electric permittivities are expressed in terms of the Atwood numbers A and A_ϵ, which are dimensionless parameters. The remaining physical quantities in the system are non-dimensionalized by $\tilde{\boldsymbol{U}}=\bar{\boldsymbol{U}}\sqrt{\frac{k}{g}}$, $\tilde{\Gamma}=\Gamma\sqrt{\frac{k^3}{g}}$, $\tilde{E}_0=E_0\sqrt{\frac{k}{g}\frac{\bar{\epsilon}}{\bar{\rho}}}$, and $\tilde{D}_0=D_0\sqrt{\frac{k}{g\bar{\epsilon}\bar{\rho}}}$. Here $\bar{\epsilon}=\frac{\epsilon_1+\epsilon_2}{2}$ and $\bar{\rho}=\frac{\rho_1+\rho_2}{2}$ are the average electric permittivity and the average density of the two fluids, respectively.

For all numerical simulations conducted in this section, the material interface is initially perturbed by a single-mode sinusoidal disturbance, i.e. $\tilde{y}_i^0=-\tilde{a}_0\cos(\tilde{x}_i^0)$, where the initial grid points $\tilde{x}_i^0$ is uniformly distributed in the interval $[-\pi,\pi]$, and $\tilde{a}_0$ is the dimensionless initial amplitude of the material interface. The perturbed material interface is static at the initial moment, namely $\tilde{\boldsymbol{U}}_i^0=0$ and $\tilde{\Gamma}_i^0=0$ for all i. Unless specified otherwise, the dimensionless physical parameters in all numerical simulations in this section are $A=0.3$, $A_\epsilon=0.5$, $\tilde{a}_0=0.1$, $\tilde{E}_0=0.5$ and $\tilde{D}_0=0$. The regularization function g_3 given by Eq. (5.2b) are used in all simulations.

7.1 Validation in the weakly nonlinear regime

In the weakly nonlinear regime, the material interface has not developed into a complicated shape yet. Therefore, the role of dynamic mesh is not essential. Hence, in each simulation, we use a fixed number of spline segments. The size of the time step is constant $\Delta t=0.001$ in all simulations. We first conduct numerical simulations with three different values of regularization factors to show the convergence of the numerical solutions under the refinement of the regularization factors. We fix $N=800$ and choose $\delta_v=\delta_e=\delta$ with $\delta=0.4$,0.3, and 0.2. Fig. 5a is the dimensionless velocity of bubbles $\tilde{v}_{\text{bb}}\equiv\tilde{U}_y(\tilde{x}=\pi)$ versus the dimensionless time $\tilde{t}$, and Fig. 5b is the dimensionless velocity of spikes $\tilde{v}_{\text{sp}}\equiv\tilde{U}_y(\tilde{x}=0)$

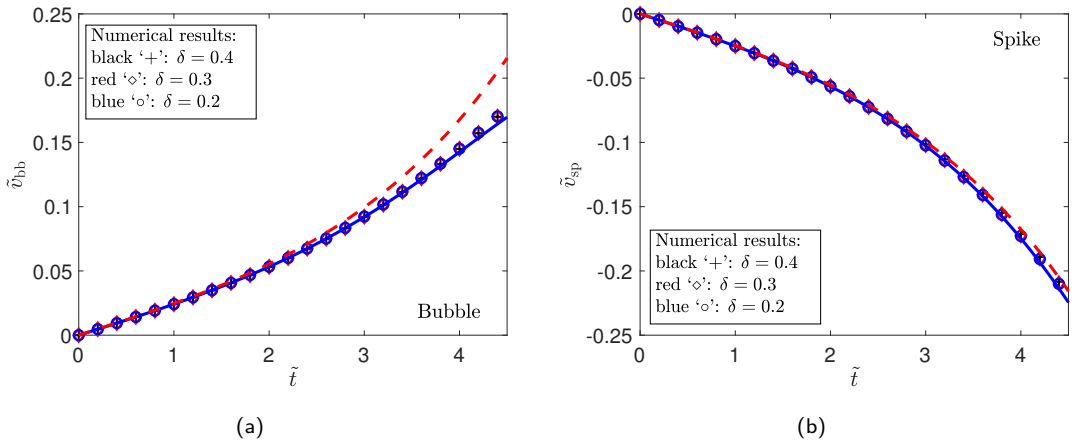

(a) (b)

Figure 5: Convergence of the dimensionless bubble/spike velocity $\tilde{v}_{\mathrm{bb/sp}}$ from the vortex spline method under the refinement of regularization factors at early times. The numerical results (black '+' for $\delta=0.4$, red '◇' for $\delta=0.3$, blue '○' for $\delta=0.2$) all coincide with each other, and converge to the linear theory (red dashed curves) within the linear regime and to the nonlinear perturbation theory (blue solid curves) within the weakly nonlinear regime. This confirms the convergence of the numerical results under the refinement of regularization factors.

versus $\tilde{t}$. The numerical results for $\delta=0.4$,0.3, and 0.2 are plotted in black '+', red '◇', and blue '○' symbols, respectively. As a base of the convergent study, we also plot the prediction of the linear theory (red curves) and that of the third-order nonlinear perturbation theory (blue curves). The linear theory gives $\tilde{v}_{\mathrm{bb}}^{\mathrm{lin}}=\tilde{a}_0\sigma\sinh(\sigma\tilde{t})$ and $\tilde{v}_{\mathrm{sp}}^{\mathrm{lin}}=-\tilde{v}_{\mathrm{bb}}^{\mathrm{lin}}$, where $\sigma=\sqrt{A-A_\epsilon^2\tilde{E}_0^2}$ [6]. The analytical expressions for the third-order nonlinear perturbation solutions are listed as Eqs. (4.8)–(4.12) in [69]. Fig. 5 shows that the results from all three numerical simulations coincide with each other. This confirms the convergence of the numerical solutions. At very early times, three numerical solutions from different regularization factors all agree with both the prediction of the linear theory and that of the nonlinear perturbation solution. However, as time proceeds, the nonlinear effects become progressively evident. Therefore, all numerical solutions gradually deviate from the prediction of the linear theory but still agree well with that of the nonlinear perturbation solution up to the weakly nonlinear stage (see Fig. 5a). This shows that the simulations capture the nonlinear behavior of the finger development at the unstable RT interface.

To confirm the convergence of numerical solutions under mesh refinement, we conduct numerical simulations with various numbers of spline segments representing the material interface, i.e. $N=200$,400,800 and 1600. The physical parameters are the same as in Fig. 5, and the size of the time step remains $\Delta t=0.001$. The regularization factor is $\delta_v=\delta_e=0.3$. Figs. 6a and 6b plot the numerical solutions for the dimensionless velocity of bubbles $\tilde{v}_{\mathrm{bb}}$ and that of spikes $\tilde{v}_{\mathrm{sp}}$, respectively. The numerical results with $N=200$,400,800, and 1600 are plotted in black '+', red '◇', blue '○', and magenta 'Δ' symbols, respectively. Fig. 6 clearly shows that all four numerical solutions with different values of N coincide with

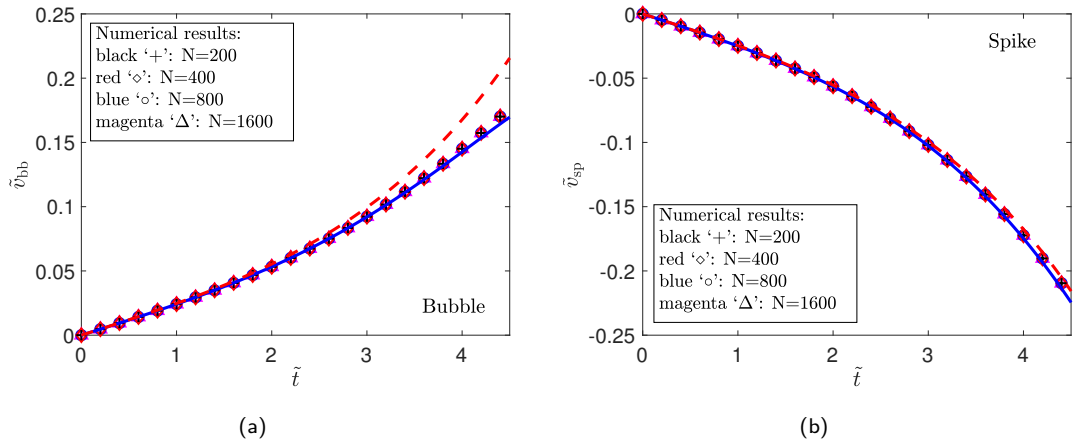

Figure 6: Convergence of the dimensionless bubble/spike velocity $\tilde{v}_{bb/sp}$ from the vortex spline method under mesh refinement at early times for four different numbers of spline segments (black '+': $N=200$; red '◇': $N=400$; blue '○': $N=800$; magenta 'Δ': $N=1600$). The results for all cases coincide with each other and agree well with the linear theory (red dashed curves) within the linear regime and with the nonlinear perturbation theory (blue solid curves) within the weakly nonlinear regime. This confirms the convergence of the numerical results under mesh refinement.

each other. It also shows that these numerical solutions all agree with the prediction of the linear theory (red curves) at early times and agree with the prediction of the nonlinear perturbation solution (blue curves) over a longer time, since the nonlinear perturbation solution takes into account the nonlinear behavior of fingers and has a longer range of validity. Even for a coarse mesh with $N=200$ spline segments, the numerical results agree with the prediction of the linear theory up to $\tilde{t}=2.5$ and with that of the nonlinear perturbation solution up to $\tilde{t}=4.5$. This shows that it is unnecessary to use a fine mesh with a large number of spline segments in the numerical simulations for the early-time evolution of the material interface. However, the situation is very different at late times, at which the material interface becomes fully nonlinear and has a complicated shape.

7.2 Validation in the fully nonlinear regime

In Section 7.1, the convergence and accuracy of the vortex spline method have been validated up to the weakly nonlinear regime. Now we carry out the validation studies further to the late-time nonlinear regime.

In Figs. 7a and 7b, we plot the numerical solutions for the dimensionless velocity of bubbles $\tilde{v}_{bb}$ and that of spikes $\tilde{v}_{sp}$ obtained from the vortex spline method with various values of regularization factors. The setting of numerical simulations and the meaning of symbols in Fig. 7 are the same as in Fig. 5 ($N=800$ and $\delta=0.4,0.3,0.2$). The simulations are conducted up to the nonlinear regime of $\tilde{t}=8.8$, after which an intersection occurs at the material interface for the case of $\delta=0.2$ due to a lacking of spline segments that represent the interface. Fig. 7 shows that the numerical solutions for the finger velocities with

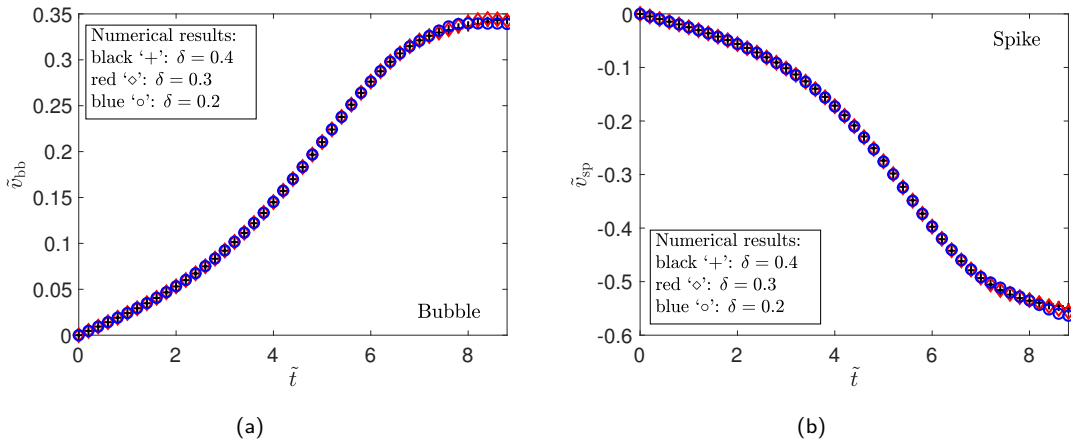

Figure 7: Convergence of the dimensionless bubble/spike velocity $\tilde{v}_{\mathrm{bb/sp}}$ from the vortex spline method under the refinement of regularization factors δ at late times. The meaning of symbols is the same as in Fig. 5. The figure shows that the numerical results are convergent to each other.

different values of regularization factors are almost identical to each other. Therefore, for the finger growth at the RT interface, which is the most important quantity in RTI problems, the vortex spline method gives convergent numerical results under the refinement of regularization factors.

In Figs. 5 and 7, we showed how the regularization factor influences the growth of fingers, which is the large-scale behavior of the material interface. Now we examine how the regularization factor affects the fine-scale features of the material interface. Plotted in Fig. 8 are the snapshots of a material interface at $\tilde{t}$=20 for a system with $\tilde{E}_0$=0.4125, A_ϵ=1/3 and a small Atwood number A=1/10 which enhances the fine-scale structures such as roll-ups. The procedure of dynamic mesh adjustment is applied and the initial number of spline segments representing the material interface is N=400. The numerical simulation in each subfigure of Fig. 8 is conducted with (a) δ=0.4, (b) δ=0.3, and (c) δ=0.2, respectively. The comparison in Fig. 8 shows that a smaller value of δ leads to more pronounced fine-scale structures at the material interface. This is consistent with the phenomena observed in [1], in which the regularization method was derived and the effects of the regularization factor were investigated comprehensively. On the other hand, as shown in Fig. 7, the large-scale structures at the material interface, namely the growth rate at the bubble tip and that at the spike tip, do not show any differences for these three values of δ. We comment that the choice of the regularization factor δ is problem-dependent. In the studies of RTI, people are mostly interested in the evolution of the mixing length, namely the vertical distance between the highest and lowest points of the material interface. For this purpose, δ=0.3 is sufficient. However, if one investigates the details of fine-scale structures at the material interface, such as the interface shape near the vortex centers, a smaller value of δ is needed.

In Figs. 9a and 9b, we show the finger velocities $\tilde{v}_{\mathrm{bb}}$ and $\tilde{v}_{\mathrm{sp}}$ for various numbers of

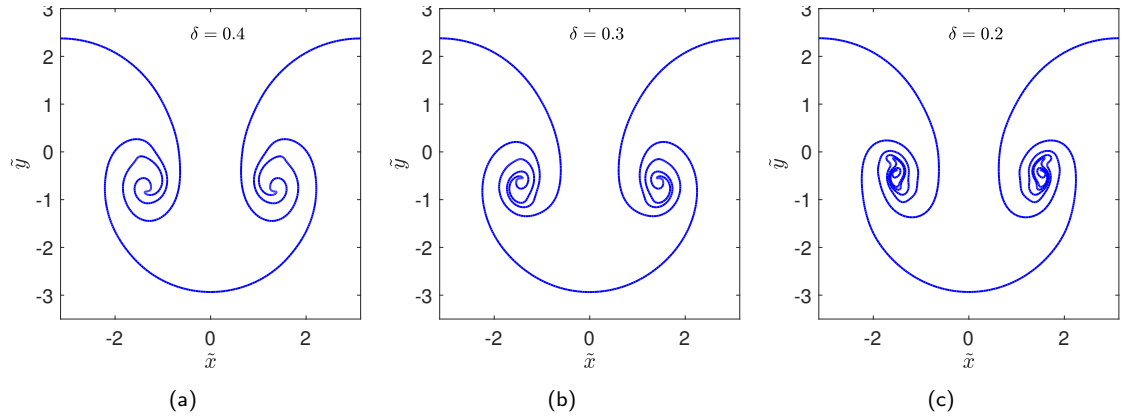

Figure 8: Comparison between the material interfaces at $\tilde{t}=20$ obtained by (a) $\delta=0.4$, (b) $\delta=0.3$, and (c) $\delta=0.2$. The figures show that a smaller regularization factor leads to more pronounced fine-scale structures at the unstable material interface, but provides almost identical results for the growth of large-scale fingers.

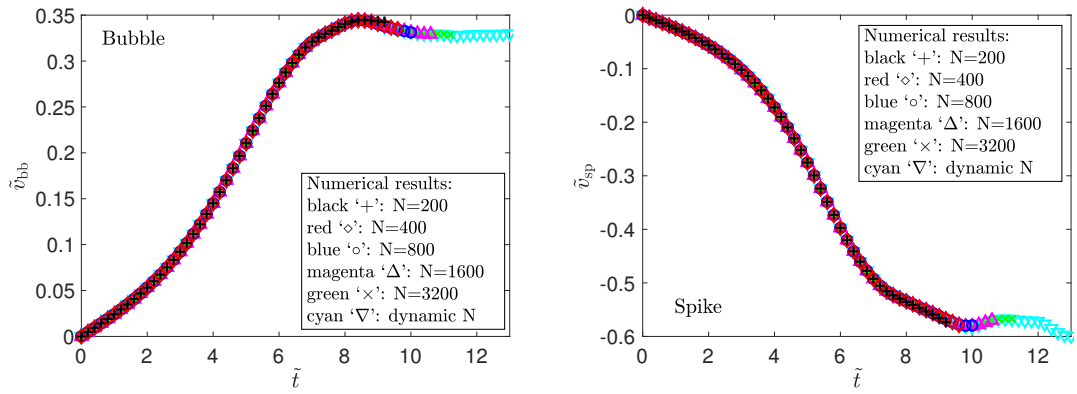

Figure 9: Convergence of the dimensionless bubble/spike velocity $\tilde{v}_{bb/sp}$ from the vortex spline method under mesh refinement at late times. Four cases with a fixed number of spline segments N are presented up to the moment when each simulation is halted due to an under-resolved mesh (black '+': $N=200$; red '◇': $N=400$; blue '○': $N=800$; magenta 'Δ': $N=1600$; green '×': $N=3200$). Additionally, the numerical results with a dynamically adjusted N (controlled by Algorithm 4) are plotted in cyan '∇' symbols until N reaches 3200. The figure shows that the numerical results for all cases coincide with each other. The figure also shows that the numerical simulation with a dynamic N runs up to a much later stage than those with a fixed N.

spline segments representing the material interface, i.e. $N=200,400,800,1600$, and 3200. Compared to Fig. 6, we double the number of spline segments up to $N=3200$ because the interface shape becomes much more complicated at late times. All physical parameters and symbols are the same as in Fig. 6, with the addition of green '×' symbols denoting the results of $N=3200$. Since the number of spline segments N is fixed during each numerical simulation, a lack of resolution at the material interface eventually occurs in the stretched

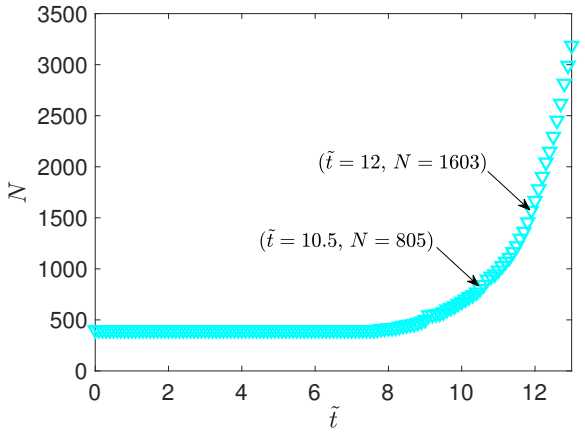

Figure 10: Number of spline segments N for the numerical simulation based on dynamic mesh adjustment in Fig. 9 versus dimensionless time $\tilde{t}$. The figure shows that dynamic mesh adjustment is more efficient since it maintains a smaller value of N compared to a fixed-mesh simulation.

and roll-up regions at late times. This can lead to an unphysical solution of the material interface that intersects with itself in numerical simulations. Hence, the above numerical results are plotted only up to the moments when an intersection occurs. Fig. 9 shows that the numerical results from different N all coincide with each other up to the occurrence of intersections. This confirms that the numerical solutions obtained from the vortex spline method are convergent under mesh refinement at late times.

As time evolves, the interface shape becomes increasingly complicated and roll-up structures emerge at the interface. Naturally, more cubic spline segments are needed to represent the shape of the interface. However, increasing the number of segments at the initial mesh is not a suitable approach to fulfill this need. This is clearly shown in Fig. 9, in which the numerical simulations with a fixed number of cubic spline segments $N=200,400,800,1600$, and 3200 halted at $\tilde{t}\approx 9.3,9.6,10.0$, 10.5, and 11.2, respectively. Thus, when we increases N by a factor of 16 (from 200 to 3200), the numerical simulation is only extended by 20% (from 9.3 to 11.2). This problem is rooted in the fact that one needs significantly more segments to represent the regions with a very complicated interface shape, but only a small number of segments to represent the regions with a relatively simple shape. In the numerical simulations with a fixed N, a large portion of segments is wasted in the latter regions, but a critical shortage of segments still occurs in the former regions. To resolve this issue, we apply a procedure of dynamic mesh adjustment to refine the mesh only where and when it is needed in the complete implementation of the vortex spline method. The details of the procedure are provided in Algorithm 4. To demonstrate its advantages, in Fig. 9 we also plot the results of a numerical simulation conducted with dynamic mesh adjustment (cyan '∇' symbols) for the same system as the fixed-N simulations in this figure. The number of spline segments is initialized by

$N=400$ and additional segments are inserted as needed during the simulation. The simulation automatically finished when N reached 3200, which is the same as the number of segments in the finest fixed mesh in the comparison. Fig. 9 shows that the dynamic mesh adjustment method carries out a longer numerical simulation than the fixed-N method. Fig. 10 displays how the number of spline segments N increases with $\tilde{t}$ in the dynamic mesh adjustment method. It shows that the value of N stays at 400 until $\tilde{t}$ reaches 7.6. Then N increases to 800 at $\tilde{t}\approx 10.5$. This is the time at which the numerical simulation with a fixed $N=1600$ halted due to the self-intersection of the interface. When N reaches 1600, the simulation further progresses to $\tilde{t}\approx 12$, which is beyond the time at which a fixed $N=3200$ failed due to self-intersection. Finally, the simulation finishes at $\tilde{t}\approx 13$ when N reaches 3200 without self-intersection. We comment that even though the results of the finger velocity from a fixed $N=3200$ and that from a dynamic N are almost identical, the one with a dynamic N has a much coarser mesh at early times and therefore is much less time-consuming than the one with a fixed N. This confirms that the dynamic mesh adjustment is more efficient and more robust than the uniform mesh refinement at the initial moment. Fig. 10 also shows that the value of N grows faster at later times. This is due to the fact that the material interface becomes increasingly more complicated and more stretched as time proceeds. Hence, the effects of dynamic mesh adjustment become more prominent as the numerical simulation reaches late times.

Fig. 11 demonstrates the convergence of the vortex spline method under the refinement of dynamic mesh. In Fig. 11, we display the material interfaces at $\tilde{t}=12$ obtained with three different dynamic meshes. All three simulations have the same initial number of spline segments $N=400$ and the same regularization factor $\delta=0.3$. In the order of Figs. 11a, 11b, and 11c, we tighten the criteria for locally refining the mesh in each simulation and consequently increase the number of spline segments N used to represent the material interface. The final numbers of N are (a) $N=1570$, (b) $N=2068$, and (c) $N=2584$. A comparison between Figs. 11a–11c shows that the material interfaces obtained with different N in these three simulations are almost identical. Only under a very close inspection of Fig. 11, the material interface with larger N exhibits slightly more pronounced fine-scale structures. This is what one would expect by the fact that the finer the mesh, the more details of the fine structures can be revealed. For practical purposes, these figures are indistinguishable. This confirms the convergence of the vortex spline method under the refinement of dynamic mesh.

We also conducted validation studies on the convergence of the vortex spline method under the refinement of time step sizes by simulating the same system shown in this section with different sizes of time steps. In the simulations with a fixed mesh, the size of the time step is fixed with $\Delta t=0.002$,0.001, and 0.0005; in the simulations with a dynamic mesh, the size of the time step is adaptively adjusted and Δt is initialized with the above three values. The numerical results obtained with these three different Δt are almost identical. All of the numerical results shown in this section are obtained with $\Delta t=0.001$.

Figs. 5–9 show the validation studies for RT systems under the effects of gravity and a horizontal external electric field. We have also conducted the same validation studies for

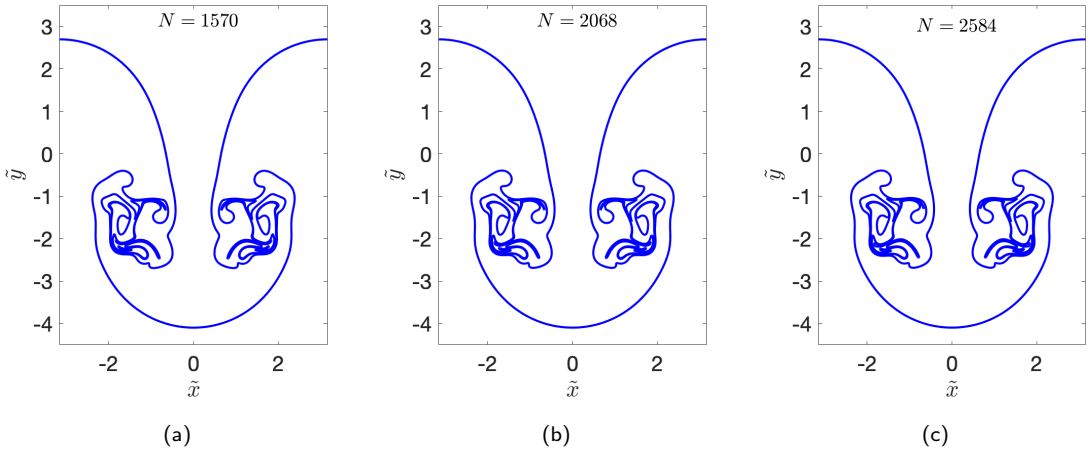

Figure 11: Comparison between the material interfaces at $\tilde{t}=12$ obtained with different dynamic meshes. From left to right, the criteria for dynamic mesh refinement in each simulation become stricter, and the number of spline segments N used to represent the material interface becomes larger consequently, i.e. (a) $N=1570$, (b) $N=2068$, and (c) $N=2584$. The figure shows that as N increases, the profile of the large-scale structures remains visually identical, and the fine-scale structures become slightly more pronounced. This validates the convergence of the vortex spline method under the refinement of dynamic mesh.

systems under the effects of gravity and a vertical external electric field. The studies show that the vortex spline method is still convergent in the presence of a vertical electric field. The resulting figures are similar to Figs. 5–9.

8 Numerical examples

In this section, we will demonstrate the capability of the vortex spline method with examples of simulating RT systems in various external electric fields. All numerical simulations are initialized with a single-mode material interface with zero velocities and a dimensionless initial amplitude $\tilde{a}_0=0.1$. The dynamic mesh adjustment is employed with an initial number of spline segments $N=400$. The regularization function is g_3 given by Eq. (5.2b) and the regularization factors are $\delta_v=\delta_e=0.3$. The size of the time step is initially $\Delta t^0=0.005$ and is adaptively adjusted during the simulations based on the CFL condition.

In Fig. 12, we display the evolution of a single-mode unstable RT interface up to the nonlinear regime under various external electric fields. In this set of numerical simulations, the Atwood number is $A=1/3$ and the dielectric Atwood number is $A_\epsilon=1/2$. We conduct three different simulations with the same initial material shape to show the effects of external electric fields: (a) in Figs. 12a–12c, a horizontal electric field is applied ($\tilde{E}_0=1/\sqrt{3}$); (b) in Figs. 12d–12f, no electric field is applied (as a basis of comparison); (c) in Figs. 12g–12i, a vertical electric field is applied ($\tilde{D}_0=1/\sqrt{3}$). For each simulation,

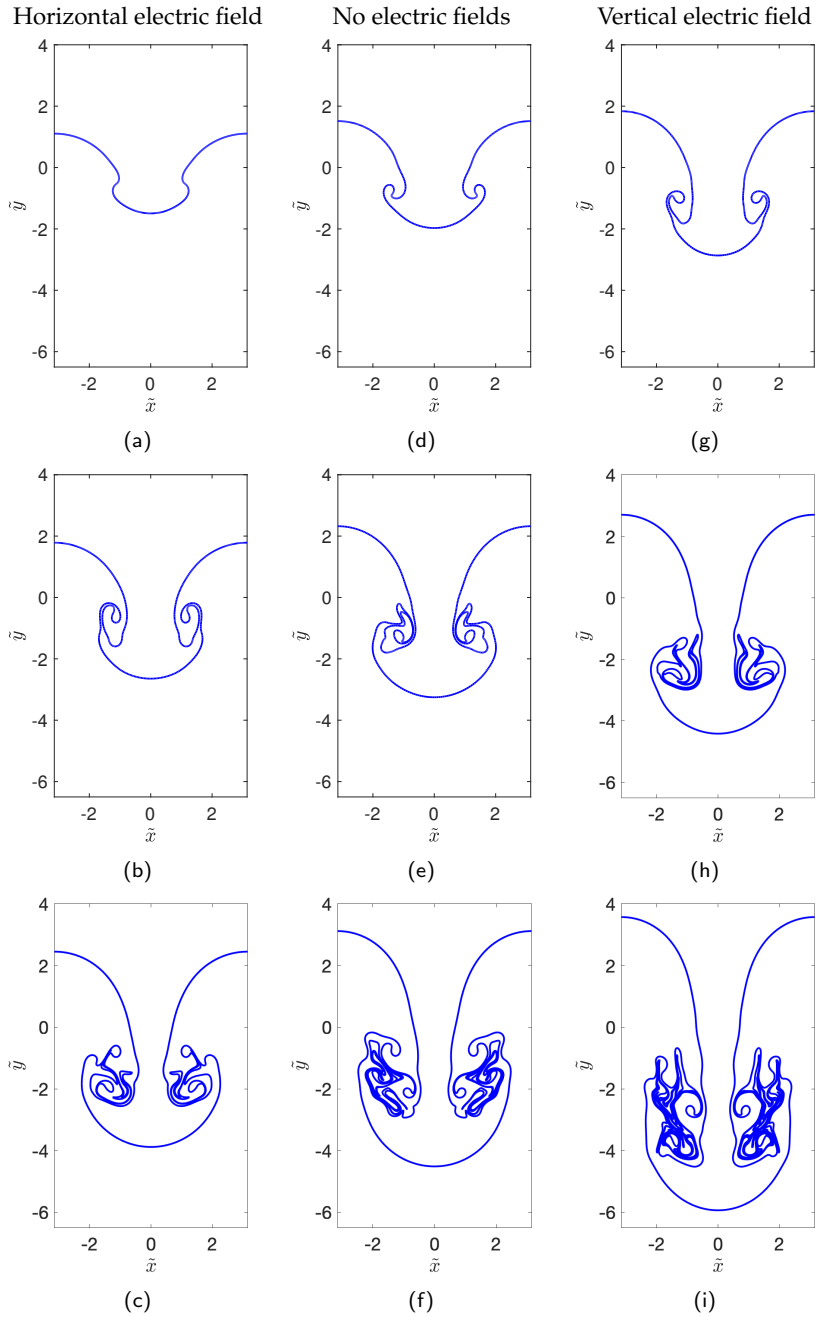

Figure 12: Evolution of a single-mode unstable RT interface in the presence of (a)-(c) a horizontal external electric field, (d)-(f) no external electric fields, and (g)-(i) a vertical external electric field. The material interfaces in all three sequences have the same initial shape. The snapshots of the material interface in each sequence are taken at $\tilde{t}=7,9$, and 11, respectively. The figure shows that the horizontal electric field suppresses the growth of both large-scale fingers and fine-scale structures, whereas the vertical electric field enhances the growth. The final number of spline segments are: (c) $N=1214$, (f) $N=2324$, (i) $N=5284$.

the snapshots of the material interface are taken sequentially at time $\tilde{t}=7,9$, and 11. The comparison among these snapshot sequences exhibits how the material interface evolves differently under different external electric fields. Compared to the case without external electric fields (Figs. 12d–12f), the horizontal electric field suppresses interfacial instability (Figs. 12a–12c) while the vertical electric field enhances finger growth (Figs. 12g–12i). Such phenomena are consistent with the numerical results in Refs. [47,48] and the linear analysis in Ref. [3]. In addition to large-scale fingers, fine-scale structures also demonstrate different features at late times (see Figs. 12c, 12f, and 12i). For example, the stabilizing effects of the horizontal electric field reduce the complexity and the rotation of the roll-up structures at the sides of the spike tip (see Figs. 12c and 12f). On the contrary, the application of a vertical electric field leads to the formation of much more complicated structures near the spike tip, and the roll-up feature of these structures becomes more prominent than those in the system without external electric fields (see Figs. 12f and 12i).

The vortex spline method can also handle systems with an external electric field oblique to the unperturbed material interface at an arbitrary angle. Our study shows that the fingers stay left-right symmetric when only a horizontal or vertical external electric field is present. One may speculate that such symmetry still holds for systems with an oblique external electric field. We now show this is not the case. In Fig. 13, we show the evolution of an RT interface with an oblique external electric field. As aforementioned, we decompose the oblique electric field into a horizontal electric field with the dimensionless strength $\tilde{E}_0$ and a vertical electric displacement field with the dimensionless strength $\tilde{D}_0$. The parameters are $\tilde{E}_0=0.6$, $\tilde{D}_0=0.8$, $A=1/20$, and $A_\epsilon=1/3$. The snapshots shown in Fig. 13 are taken sequentially at $\tilde{t}=10,12$, and 14. Although the bubbles and spikes in Fig. 13 still exhibit the penetration characteristics during the evolution, the penetration of these fingers is no longer symmetric despite the symmetry of the initial shape. The material interface in Fig. 13 exhibits a "shearing" behavior, similar to the Kelvin-Helmholtz instability that occurs when a velocity difference exists across the material interface between two fluids. In Fig. 13, the shearing develops as an asymmetric horizontal motion of large-scale structures, i.e. the bubble moves to the right and the spike moves to the left. This shearing enhances the fluid mixing in one of the two roll-up centers (see the dashed box in Fig. 13c) and reduces the other.

In this paper, we focus on systems with the property of periodicity in the horizontal direction. This is a common setting for the studies of RTI. The extension of the presented vortex method to a more general setting depends on the specific situation. For example, it is straightforward to extend the method to a two-fluid flow in which the material interface between the two fluids is a closed curve. In this case, one only needs to evaluate the velocity of the material interface and the average electric displacement at the material interface using Eqs. (5.5) and (5.6), instead of Eqs. (5.3) and (5.4). However, for systems containing non-fluid interfaces, such as walls, the formulation will become much more complicated. Based on the boundary conditions at these walls, one needs to determine the vortices along the walls and calculate the contributions from these vortices to the material interface. We comment that the vortices at the walls also evolve dynamically. This is a

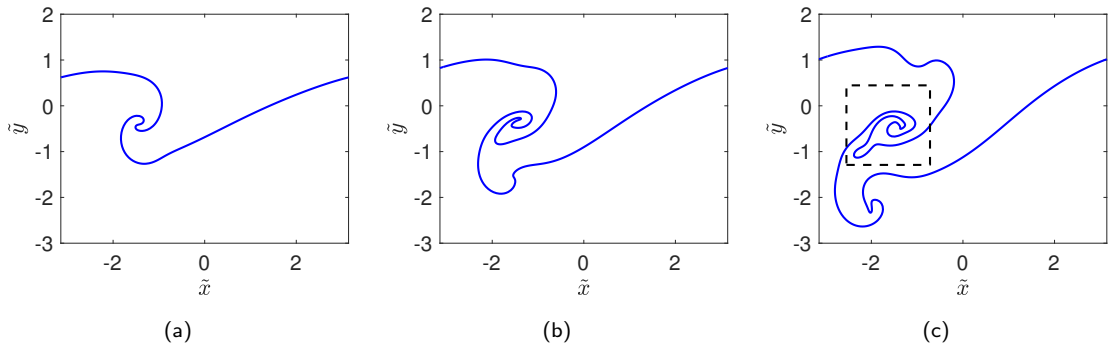

Figure 13: Evolution of a single-mode unstable RT interface in the presence of both horizontal and vertical electric fields. The figure shows that the bubbles and the spikes exhibit asymmetric motion in the horizontal direction due to the external electric fields. This enhances the fluid mixing at the material interface (see the dashed box in figure (c)).

difficult task even for the classical RTI systems without external electric fields. Therefore, it is beyond the scope of this work for electrohydrodynamics systems.

9 Conclusion

In this paper, we present a numerical method for simulating material interfaces between incompressible, inviscid, and perfect dielectric fluids in the presence of gravity and external electric fields. Based on the vortex formulation, the velocity field and the electric displacement field of the system are both formulated by vortex sheets confined to the material interface. The dynamics of the entire system is governed by the equations of the vortex sheets, and the numerical computation is only performed at the one-dimensional material interface instead of in the two-dimensional domain. We validate the convergence of the numerical solutions obtained from the vortex spline method. By comparing the numerical solutions with the predictions of the theories in the literature, we show that the vortex spline method provides accurate results for the growth of fingers. Numerical examples for simulating unstable RT interfaces in the presence of various external electric fields are included. We comment that while the examples in this paper focus on material interfaces with a single-mode initial perturbation and periodic boundary conditions, the vortex spline method is also applicable to multi-mode interfaces and to non-periodic systems. Moreover, the vortex spline method can be extended to interfacial mixing problems other than RTI, including Richtmyer-Meshkov instability and Kelvin-Helmholtz instability, in the presence of external electric fields.

Surface tension plays an important role in the dynamics of unstable interfaces [50]. However, the inclusion of surface tension can introduce numerical instability and difficulties to vortex methods [70–72]. Further investigation is still required to incorporate the effects of surface tension into the vortex spline method.

Acknowledgments

The work of Q.Z. was supported in part by the National Natural Science Foundation of China (grant number 12272054); in part by the Guangdong Provincial Key Laboratory of IRADS (project number 2022B1212010006); and in part by Guangdong Higher Education Upgrading Plan (2021-2025) with No. of UICR0400024-21 at Beijing Normal-Hong Kong Baptist University, Zhuhai, China.

A Derivation of Eqs. (3.8b) and (3.8c) in vortex formulation

Based on vortex formulation, an RT system of incompressible, inviscid and perfect dielectric fluids with external electric fields is governed by Eq. (3.8). In particular, Eq. (3.8a) describes the motion of the material interface, and Eqs. (3.8d) and (3.8e) are derived from the Birkhoff–Rott integral. In this appendix, we provide the derivation of the two remaining equations, namely Eq. (3.8b) that governs the evolution of vorticity and Eq. (3.8c) that governs the electric displacement field at the interface.

To evaluate the average electric displacement $\bar{\boldsymbol{D}}$ at the material interface, one needs to determine the induced polarization charge β at the interface. We derive Eq. (3.8c) for the determination of β. This can be obtained from Eq. (2.8b), i.e.

$$\left(\frac{\boldsymbol{D_1}}{\epsilon_1}-\frac{\boldsymbol{D_2}}{\epsilon_2}\right)\cdot\hat{\boldsymbol{s}}=0. \tag{A.1}$$

Since $\beta=(\boldsymbol{D_1}-\boldsymbol{D_2})\cdot\hat{\boldsymbol{s}}$ and $\bar{\boldsymbol{D}}=(\boldsymbol{D_1}+\boldsymbol{D_2})/2$, $\boldsymbol{D_1}$ and $\boldsymbol{D_2}$ can be expressed as

$$\boldsymbol{D_1}=\bar{\boldsymbol{D}}+\frac{1}{2}\beta\hat{\boldsymbol{s}} \quad \text{and} \quad \boldsymbol{D_2}=\bar{\boldsymbol{D}}-\frac{1}{2}\beta\hat{\boldsymbol{s}}. \tag{A.2}$$

After substituting Eq. (A.2) into Eq. (A.1), we obtain

$$\left(\frac{1}{\epsilon_1}-\frac{1}{\epsilon_2}\right)\bar{\boldsymbol{D}}\cdot\hat{\boldsymbol{s}}+\left(\frac{1}{\epsilon_1}+\frac{1}{\epsilon_2}\right)\frac{\beta}{2}=0. \tag{A.3}$$

In terms of $A_\epsilon=(\epsilon_2-\epsilon_1)/(\epsilon_2+\epsilon_1)$, Eq. (A.3) can be simplified into Eq. (3.8c), i.e.

$$\beta+2A_\epsilon\bar{\boldsymbol{D}}\cdot\hat{\boldsymbol{s}}=0. \tag{A.4}$$

Now we derive Eq. (3.8b), namely the evolution equation for the vorticity Γ confined to the material interface. Eq. (2.12) shows that

$$p_1-p_2=\frac{1}{\epsilon_1}\left[(\boldsymbol{D_1}\cdot\hat{\boldsymbol{n}})^2-\frac{1}{2}|\boldsymbol{D_1}|^2\right]-\frac{1}{\epsilon_2}\left[(\boldsymbol{D_2}\cdot\hat{\boldsymbol{n}})^2-\frac{1}{2}|\boldsymbol{D_2}|^2\right]. \tag{A.5}$$

After substituting Eq. (A.2) into Eq. (A.5), Eq. (A.5) can be rewritten in terms of $\beta,\bar{D}_x$, and $\bar{D}_y$:

$$\begin{aligned} p_1-p_2 &= \frac{1}{\epsilon_1}\left(D_n^2-\frac{1}{2}\left[D_n^2+\left(D_s+\frac{\beta}{2}\right)^2\right]\right)-\frac{1}{\epsilon_2}\left(D_n^2-\frac{1}{2}\left[D_n^2+\left(D_s-\frac{\beta}{2}\right)^2\right]\right) \\ &= \frac{1}{2\epsilon_1\epsilon_2}\left[(\epsilon_2-\epsilon_1)\left(D_n^2-D_s^2-\frac{\beta^2}{4}\right)-(\epsilon_2+\epsilon_1)\beta D_s\right] \qquad \text{(A.6)} \\ &= \frac{\epsilon_2-\epsilon_1}{2\epsilon_1\epsilon_2}\left(D_n^2+D_s^2-\frac{\beta^2}{4}\right)=\frac{\epsilon_2-\epsilon_1}{2\epsilon_1\epsilon_2}\left(\bar{D}_x^2+\bar{D}_y^2-\frac{\beta^2}{4}\right). \qquad \text{(A.7)} \end{aligned}$$

In the above equations, $D_n\equiv\bar{\boldsymbol{D}}\cdot\hat{\boldsymbol{n}}$ and $D_s\equiv\bar{\boldsymbol{D}}\cdot\hat{\boldsymbol{s}}$ are the normal and tangential components of the average electric displacement $\bar{\boldsymbol{D}}$ at the material interface, respectively. Note that we have used Eq. (A.4) during the simplification of Eq. (A.6).

From $\gamma=(\boldsymbol{u_1}-\boldsymbol{u_2})\cdot\hat{\boldsymbol{s}}$ and $\bar{\boldsymbol{U}}=(\boldsymbol{u_1}+\boldsymbol{u_2})/2$, one can rewrite the velocity vector and the acceleration vector of fluid i ($i=1,2$) as

$$\boldsymbol{u_i}=\bar{\boldsymbol{U}}+\frac{(-1)^{i-1}}{2}\gamma\hat{\boldsymbol{s}} \quad \text{and} \quad \boldsymbol{a_i}=\frac{d\boldsymbol{u_i}}{dt}+\frac{(-1)^{i-1}}{2}\gamma\frac{\partial\boldsymbol{u_i}}{\partial s}, \qquad \text{(A.8)}$$

where

$$\frac{d}{dt}\equiv\frac{\partial}{\partial t}+\bar{\boldsymbol{U}}\cdot\nabla \qquad \text{(A.9)}$$

is the material derivative following the motion of the interface. Based on the Euler equation $\rho_i\boldsymbol{a_i}=-\nabla p_i-\rho_i g\hat{\boldsymbol{j}}$, taking the difference in the tangential accelerations across the material interface gives

$$(\boldsymbol{a_1}-\boldsymbol{a_2})\cdot\hat{\boldsymbol{s}}=A(\boldsymbol{a_1}+\boldsymbol{a_2})\cdot\hat{\boldsymbol{s}}+2Ag\hat{\boldsymbol{j}}\cdot\hat{\boldsymbol{s}}-\frac{2}{\rho_1+\rho_2}\frac{\partial(p_1-p_2)}{\partial s}, \qquad \text{(A.10)}$$

where $A=(\rho_2-\rho_1)/(\rho_2+\rho_1)$. Substituting Eqs. (A.7) and (A.8) into Eq. (A.10), we obtain the evolution equation for the vortex sheet strength γ, i.e.

$$\frac{d\gamma}{dt}+\gamma\frac{\partial\bar{\boldsymbol{U}}}{\partial s}\cdot\hat{\boldsymbol{s}}=2A\frac{d\bar{\boldsymbol{U}}}{dt}\cdot\hat{\boldsymbol{s}}+2Ag\frac{\partial y}{\partial s}-\frac{\partial F_\gamma}{\partial s}-\frac{\partial F_e}{\partial s}, \qquad \text{(A.11)}$$

where $F_\gamma=-\frac{A}{4}\gamma^2$ and $F_e=\frac{\epsilon_2-\epsilon_1}{\epsilon_1\epsilon_2(\rho_1+\rho_2)}\left(\bar{D}_x^2+\bar{D}_y^2-\frac{\beta^2}{4}\right)$. We comment that when $F_e=0$, i.e. when the external electric field is absent or when the electric permittivities of the two fluids are equal, Eq. (A.11) reduces to the equation for γ in the classical RTI problem.

Eq. (A.11) is the evolution equation for the vortex strength of velocity γ. To construct a numerical scheme that preserves vorticity, we rewrite Eq. (A.11) as an evolution equation for the vorticity. Consider an arbitrary segment of the material interface whose Lagrangian coordinate ranges from α^- to α^+. The vorticity that the segment holds is

$\Gamma=\int_{s(\alpha^-)}^{s(\alpha^+)}\gamma(s,t)ds=\int_{\alpha^-}^{\alpha^+}\gamma(\alpha,t)\frac{\partial s}{\partial\alpha}d\alpha$. Taking the derivative of this equation with respect to t gives

$$\frac{d\Gamma}{dt}=\frac{d}{dt}\int_{\alpha^-}^{\alpha^+}\gamma(\alpha,t)\frac{\partial s}{\partial\alpha}d\alpha=\int_{\alpha^-}^{\alpha^+}\frac{\partial}{\partial t}\left(\gamma(\alpha,t)\frac{\partial s}{\partial\alpha}\right)\Big|_{\alpha}d\alpha, \tag{A.12}$$

where $\frac{\partial}{\partial t}(\cdot)\Big|_{\alpha}$ denotes the time derivative of a variable taken with the Lagrangian coordinate α fixed. In Eq. (A.12), the time derivative and the integration are exchangeable since the Lagrangian coordinate does not change with time. The integrand on the right-hand side of Eq. (A.12) can be written as

$$\frac{\partial}{\partial t}\left(\gamma(\alpha,t)\frac{\partial s}{\partial\alpha}\right)\Big|_{\alpha}=\frac{d\gamma}{dt}\frac{\partial s}{\partial\alpha}+\gamma\frac{\partial}{\partial t}\left(\frac{\partial s}{\partial\alpha}\right)\Big|_{\alpha}. \tag{A.13}$$

Since

$$\begin{aligned}\frac{\partial}{\partial t}\left(\frac{\partial s}{\partial\alpha}\right)\Big|_{\alpha}&=\frac{\partial}{\partial t}\left[\left(\frac{\partial x}{\partial\alpha}\right)^2+\left(\frac{\partial y}{\partial\alpha}\right)^2\right]^{\frac{1}{2}}\Big|_{\alpha}\\&=\left[\left(\frac{\partial x}{\partial\alpha}\right)^2+\left(\frac{\partial y}{\partial\alpha}\right)^2\right]^{-\frac{1}{2}}\left[\frac{\partial x}{\partial\alpha}\frac{\partial}{\partial t}\left(\frac{\partial x}{\partial\alpha}\right)\Big|_{\alpha}+\frac{\partial y}{\partial\alpha}\frac{\partial}{\partial t}\left(\frac{\partial y}{\partial\alpha}\right)\Big|_{\alpha}\right]\\&=\frac{\partial x}{\partial s}\frac{\partial\bar{U}_x}{\partial\alpha}+\frac{\partial y}{\partial s}\frac{\partial\bar{U}_y}{\partial\alpha}\\&=\hat{\boldsymbol{s}}\cdot\frac{\partial\bar{\boldsymbol{U}}}{\partial\alpha}=\hat{\boldsymbol{s}}\cdot\frac{\partial\bar{\boldsymbol{U}}}{\partial s}\frac{\partial s}{\partial\alpha},\end{aligned} \tag{A.14}$$

substituting Eqs. (A.14), (A.11), and (A.13) into Eq. (A.12) gives Eq. (3.8b), i.e.

$$\begin{aligned}\frac{d\Gamma}{dt}&=\int_{\alpha^-}^{\alpha^+}\left(2A\frac{d\bar{\boldsymbol{U}}}{dt}\cdot\hat{\boldsymbol{s}}+2Ag\frac{\partial y}{\partial s}-\frac{\partial F_\gamma}{\partial s}-\frac{\partial F_e}{\partial s}\right)\frac{\partial s}{\partial\alpha}d\alpha\\&=2A\int_{s(\alpha^-)}^{s(\alpha^+)}\frac{d\bar{\boldsymbol{U}}}{dt}\cdot\hat{\boldsymbol{s}}ds+(2Agy-F_\gamma-F_e)\Big|_{\alpha^-}^{\alpha^+}.\end{aligned}$$

References

[1] Gregory R. Baker and J. Thomas Beale. Vortex blob methods applied to interfacial motion. *J. Comput. Phys.*, 196(1):233–258, 2004.

[2] Lord Rayleigh. Investigation of the character of the equilibrium of an incompressible heavy fluid of variable density. *Proc. London Math. Soc.*, 14:170–177, 1883.

[3] G I Taylor and A D McEwan. The stability of a horizontal fluid interface in a vertical electric field. *J. Fluid Mech.*, 22(1):1–15, 1965.

[4] James R Melcher and E Paul Warren. Continuum feedback control of a Rayleigh-Taylor type instability. *Phys. Fluids*, 9(11):2085–2094, 1966.

[5] Abou El Magd A Mohamed and Sayed F El Shehawey El. Nonlinear electrohydrodynamic Rayleigh–Taylor instability. Part 1. A perpendicular field in the absence of surface charges. *J. Fluid Mech.*, 129(1):473–494, 1983.
[6] Nabil T Eldabe. Effect of a tangential electric field on Rayleigh-Taylor instability. *J. Phys. Soc. Japan*, 58(1):115–120, 1989.
[7] V M Korovin. Effect of tangential electric field on the evolution of the Rayleigh-Taylor instability of a dielectric liquid film. *Tech. Phys+.*, 56(10):1390–1397, 2011.
[8] Lyudmyla L Barannyk, Demetrios T Papageorgiou, and Peter G Petropoulos. Suppression of Rayleigh-Taylor instability using electric fields. *Math. Comput. Simulat.*, 82(6):1008–1016, 2012.
[9] D W Moore. On the point vortex method. *SIAM J. Sci. Stat. Comput*, 2(1):65–84, 1981.
[10] Gregory R Baker, Daniel I Meiron, and Steven A Orszag. Generalized vortex methods for free-surface flow problems. *J. Fluid Mech.*, 123:477–501, 1982.
[11] Gregory R Baker, Daniel I Meiron, and Steven A Orszag. Vortex simulations of the Rayleigh–Taylor instability. *Phys. Fluids*, 23(8):1485–1490, 1980.
[12] Robert M Kerr. Simulation of Rayleigh-Taylor flows using vortex blobs. *J. Comput. Phys.*, 76 (1):48–84, 1988.
[13] Sung-Ik Sohn. Vortex model and simulations for Rayleigh-Taylor and Richtmyer-Meshkov instabilities. *Phys. Rev. E*, 69(3):036703, 2004a.
[14] A Rikanati, U Alon, and D Shvarts. Vortex model for the nonlinear evolution of the multimode Richtmyer-Meshkov instability at low Atwood numbers. *Phys. Rev. E*, 58(6):7410–7418, 1998.
[15] Sung-Ik Sohn. Vortex simulations of impulsively accelerated unstable interface. *Math. Comput. Model.*, 40(5-6):627–636, 2004b.
[16] G Taylor. The instability of liquid surfaces when accelerated in a direction perpendicular to their planes. I. *Proc. R. Soc. Lond. A*, 201(1065):192–196, 1950.
[17] Ralph Menikoff and Charles Zemach. Rayleigh-Taylor instability and the use of conformal maps for ideal fluid flow. *J. Comput. Phys.*, 51(1):28–64, 1983.
[18] K I Read. Experimental investigation of turbulent mixing by Rayleigh-Taylor instability. *Physica D*, 12:45–58, 1984.
[19] David L Youngs. Numerical simulation of turbulent mixing by Rayleigh-Taylor instability. *Physica D*, 12(1-3):32–44, 1984.
[20] Grétar Tryggvason. Numerical simulations of the Rayleigh-Taylor instability. *J. Comput. Phys.*, 75(2):253–282, 1988.
[21] J W Jacobs and I Catton. Three-dimensional Rayleigh-Taylor instability Part 1. Weakly nonlinear theory. *J. Fluid Mech.*, 187:329–352, 1988a.
[22] Jeffrey W Jacobs and I Catton. Three-dimensional Rayleigh-Taylor instability Part 2. Experiment. *J. Fluid Mech.*, 187:353–371, 1988b.
[23] Juan A Zufiria. Vortex-in-cell simulation of bubble competition in a Rayleigh–Taylor instability. *Phys. Fluids*, 31(11):3199–3212, 1988.
[24] Jacob Hecht, Uri Alon, and Dov Shvarts. Potential flow models of Rayleigh–Taylor and Richtmyer–Meshkov bubble fronts. *Phys. Fluids*, 6:4019–4030, 1994.
[25] J Hecht, D Ofer, U Alon, D Shvarts, S A Orszag, and R L McCrory. Three-dimensional simulations and analysis of the nonlinear stage of the Rayleigh-Taylor instability. *Laser Part. Beams*, 13(3):423–440, 1995.
[26] G Dimonte and M Schneider. Turbulent Rayleigh-Taylor instability experiments with variable acceleration. *Phys. Rev. E*, 54(4):3740–3743, 1996.
[27] Karnig O Mikaelian. Analytic approach to nonlinear Rayleigh-Taylor and Richtmyer-

Meshkov instabilities. *Phys. Rev. Lett.*, 80(3):508–511, 1998.
[28] Qiang Zhang. Analytical solutions of Layzer-type approach to unstable interfacial fluid mixing. *Phys. Rev. Lett.*, 81(16):3391–3394, 1998.
[29] P Ramaprabhu and M J Andrews. Experimental investigation of Rayleigh–Taylor mixing at small Atwood numbers. *J. Fluid Mech.*, 502:233–271, 1999.
[30] J T Waddell, C E Niederhaus, and J W Jacobs. Experimental study of Rayleigh–Taylor instability: Low Atwood number liquid systems with single-mode initial perturbations. *Phys. Fluids*, 13(5):1263, 2001.
[31] V N Goncharov. Analytical model of nonlinear, single-mode, classical Rayleigh-Taylor instability at arbitrary Atwood numbers. *Phys. Rev. Lett.*, 88(13):134502, 2002.
[32] Karnig Mikaelian. Explicit expressions for the evolution of single-mode Rayleigh-Taylor and Richtmyer-Meshkov instabilities at arbitrary Atwood numbers. *Phys. Rev. E*, 67(2):026319, 2003.
[33] Sung-Ik Sohn. Simple potential-flow model of Rayleigh-Taylor and Richtmyer-Meshkov instabilities for all density ratios. *Phys. Rev. E*, 67(2):026301, 2003.
[34] P Ramaprabhu and Guy Dimonte. Single-mode dynamics of the Rayleigh-Taylor instability at any density ratio. *Phys. Rev. E*, 71(3):036314, 2005.
[35] J P Wilkinson and J W Jacobs. Experimental study of the single-mode three-dimensional Rayleigh-Taylor instability. *Phys. Fluids*, 19(12):124102, 2007.
[36] P Ramaprabhu, Guy Dimonte, P Woodward, C Fryer, G Rockefeller, K Muthuraman, P H Lin, and J Jayaraj. The late-time dynamics of the single-mode Rayleigh-Taylor instability. *Phys. Fluids*, 24(7):074107, 2012.
[37] Qiang Zhang and Wenxuan Guo. Universality of finger growth in two-dimensional Rayleigh–Taylor and Richtmyer–Meshkov instabilities with all density ratios. *J. Fluid Mech.*, 786:47–61, 2016.
[38] Wenxuan Guo and Qiang Zhang. Universality and scaling laws among fingers at Rayleigh–Taylor and Richtmyer–Meshkov unstable interfaces in different dimensions. *Physica D*, 403: 132304, 2020.
[39] David H Sharp. An overview of Rayleigh-Taylor instability. *Physica D*, 12(1):3–18, 1984.
[40] Ye Zhou. Rayleigh–Taylor and Richtmyer–Meshkov instability induced flow, turbulence, and mixing. I. *Phys. Rep.*, 720-722:1–136, 2017a.
[41] Ye Zhou. Rayleigh–Taylor and Richtmyer–Meshkov instability induced flow, turbulence, and mixing. II. *Phys. Rep.*, 723-725:1–160, 2017b.
[42] A J Babchin, A L Frenkel, B G Levich, and G I Sivashinsky. Nonlinear saturation of Rayleigh–Taylor instability in thin films. *Phys. Fluids*, 26(11):3159–3161, 1983.
[43] David Halpern and Alexander L Frenkel. Saturated Rayleigh–Taylor instability of an oscillating couette film flow. *J. Fluid Mech.*, 446:67–93, 2001.
[44] N Rudraiah, B S Krishnamurthy, A S Jalaja, and Tara Desai. Effect of a magnetic field on the growth rate of the Rayleigh–Taylor instability of a laser-accelerated thin ablative surface. *Laser Part. Beams*, 22(1):29–33, 2004.
[45] James R Melcher. Electrohydrodynamic and magnetohydrodynamic surface waves and instabilities. *Phys. Fluids*, 4(11):1348–1354, 1961.
[46] James R Melcher and Wilfred J Schwarz. Interfacial relaxation overstability in a tangential electric field. *Phys. Fluids*, 11(12):2604–2614, 1968.
[47] Radu Cimpeanu, Demetrios T Papageorgiou, and Peter G Petropoulos. On the control and suppression of the Rayleigh-Taylor instability using electric fields. *Phys. Fluids*, 26(2): 022105–022121, 2014.

[48] Qingzhen Yang, Ben Q Li, Zhengtuo Zhao, Jinyou Shao, and Feng Xu. Numerical analysis of the Rayleigh–Taylor instability in an electric field. *J. Fluid Mech.*, 792:397–434, 2016.
[49] Chihiro Matsuoka and Katsunobu Nishihara. Fully nonlinear evolution of a cylindrical vortex sheet in incompressible Richtmyer–Meshkov instability. *Phys. Rev. E*, 73(5):101–104, 2006.
[50] Chihiro Matsuoka. Vortex sheet motion in incompressible Richtmyer–Meshkov and Rayleigh–Taylor instabilities with surface tension. *Phys. Fluids*, 21(9):092107, 2009.
[51] IP Christiansen. Numerical simulation of hydrodynamics by the method of point vortices. *J. Comput. Phys.*, 13(3):363–379, 1973.
[52] R D Richtmyer. Taylor instability in shock acceleration of compressible fluids. *Commun. Pure Appl. Math.*, 13:297–319, 1960.
[53] E E Meshkov. Instability of the interface of two gases accelerated by a shock wave. *Fluid Dyn.*, 4(0015-4628):101–104, 1969.
[54] D W Moore. The spontaneous appearance of a singularity in the shape of an evolving vortex sheet. *Proc. Roy. Soc. London*, 365(1720):105–119, 1979.
[55] Daniel I. Meiron, Gregory R. Baker, and Steven A. Orszag. Analytic structure of vortex sheet dynamics. Part 1. Kelvin–Helmholtz instability. *J. Fluid Mech.*, 114(1):283–298, 1982.
[56] Robert Krasny. A study of singularity formation in a vortex sheet by the point-vortex approximation. *J. Fluid Mech.*, 167(1):65–93, 1986a.
[57] Robert Krasny. Desingularization of periodic vortex sheet roll-up. *J. Comput. Phys.*, 65(2): 292–313, 1986b.
[58] JT Beale and A Majda. High order accurate vortex methods with explicit velocity kernels. *J. Comput. Phys.*, 58:188–208, 1985.
[59] Suyeon Shin, Sung-Ik Sohn, and Woonjae Hwang. Vortex simulations of the Kelvin–Helmholtz instability with surface tension in density-stratified flows. *Eur. J. Mech. B. Fluids*, 67:168–177, 2018.
[60] Suyeon Shin, Sung-Ik Sohn, and Woonjae Hwang. Numerical simulation of single- and multi-mode Rayleigh–Taylor instability with surface tension in two dimensions. *Eur. J. Mech. B. Fluids*, 91:141–151, 2022.
[61] H von Helmholtz. Über integrale der hydrodynamischen gleichungen, welche den wirbelbewegungen entsprechen. pages 25–55, 1858.
[62] Subrahmanyan Chandrasekhar. *Hydrodynamic and Hydromagnetic Stability*. Courier Corporation, 2013.
[63] Gregory Baker, Russel E Caflisch, and Michael Siegel. Singularity formation during Rayleigh–Taylor instability. *J. Fluid Mech.*, 252:51–78, 1993.
[64] S. K. Godunov. A difference scheme for numerical solution of discontinuous solution of hydrodynamic equations. *Math. Sbornik*, 47:271–306, 1959.
[65] Bram Van Leer. Towards the ultimate conservative difference scheme. V. A second-order sequel to Godunov's method. *J. Comput. Phys.*, 32(1):101–136, 1979.
[66] Xu-Dong Liu, Stanley Osher, and Tony Chan. Weighted essentially non-oscillatory schemes. *J. Comput. Phys.*, 115(1):200–212, 1994.
[67] Guang-Shan Jiang and Chi-Wang Shu. Efficient implementation of weighted ENO schemes. *J. Comput. Phys.*, 126(1):202–228, 1996.
[68] Robert Krasny. Computation of vortex sheet roll-up in the Trefftz plane. *J. Fluid Mech.*, 184(1): 123–155, 1987.
[69] Wenxuan Guo, Qiang Zhang, and Dongdong He. On the nonlinear behaviour of the Rayleigh–Taylor instability with a tangential electric field for inviscid and perfect dielectric fluids. *J. Fluid Mech.*, 958:A36, 2023.

[70] Gregory Baker and André Nachbin. Stable methods for vortex sheet motion in the presence of surface tension. *SIAM J. Sci. Comput.*, 19(5):1737–1766, 1998.
[71] J Thomas Beale, Thomas Y Hou, and John Lowengrub. Convergence of a boundary integral method for water waves. *SIAM J. Numer. Anal*, 33(5):1797–1843, 1996.
[72] J T Beale, T Y Hou, J S Lowengrub, and M J Shelley. Spatial and temporal stability issues for interfacial flows with surface tension. *Math. Comput. Model.*, 20:1–27, 1994.